# LIGHT SCATTERING OF SEMITRANSPARENT MEDIA

A Thesis
Presented to
The Academic Faculty

by

Qinghe Li

In Partial Fulfillment
of the Requirements for the Degree
Master of Science in the
School of Mechanical Engineering

Georgia Institute of Technology
May 2008

# LIGHT SCATTERING OF SEMITRANSPARENT MEDIA

Approved by:

Dr. Zhuomin Zhang, Advisor
School of Mechanical Engineering
*Georgia Institute of Technology*

Dr. Kok-Meng Lee
School of Mechanical Engineering
*Georgia Institute of Technology*

Dr. W. Jud Ready
Georgia Tech Research Institute
*Georgia Institute of Technology*

Date Approved: 03/25/2008

ACKNOWLEDGEMENTS

I wish to thank my advisor, Dr. Zhuomin Zhang, for his guidance, support, and encouragement in this project. It was with his instructive inputs that I was able to successfully finish the project as well as maintain the quality. Thanks go to my thesis committee members, Dr. Kok-Meng Lee and Dr. W. Jud Ready, for their willingness to serve on my committee and providing valuable suggestions in various aspects of my work.

I want to thank all the group members for their friendship and help. Dr. Yu-Bin Chen helped me settle down in Atlanta. Mr. Soumyadipta Basu shared with me a lot of happiness in life and study. Dr. Keunhan Park encouraged me in research with helpful advices. Dr. Bong Jae Lee shared with me not only his information of good restaurants in Atlanta but also his philosophy in research. I also thank Dr. Lee for his cooperation in this project. Thanks go to Ms. Xiaojia Wang, Mr. Andrew McNamara and Mr. Liping Wang for their friendship and supports.

Thanks go to Mr. David W. Allen and Dr. Benjamin K. Tsai from National Institute of Standards and Technology (NIST) for their inputs in this project. Partial support from the Optical Technology Division of NIST is also appreciated.

I am indebted to my family and my fiancée, Huaiyu Zhang, for their love, support, and patience through all these years. Without them, I could not go this far.

# TABLE OF CONTENTS

# LIST OF TABLES

# LIST OF FIGURES

# LIST OF SYMBOLS

| | |
|---|---|
| $A$ | absorption coefficient of the diffuse flux in the three-flux model |
| $a$ | absorption coefficient of the collimated flux in the three-flux model |
| $d$ | film thickness |
| $E$ | energy of photon bundles |
| $F$ | reflected radiance of a Lambertian diffuser |
| $F_1, F_2, F_3$ | radiative heat fluxes in the three-flux model |
| $f_r$ | bidirectional reflectance distribution function |
| $f_t$ | bidirectional transmittance distribution function |
| $g$ | asymmetric parameter of the Henyey-Greenstein phase function |
| $h$ | redistribution function in the adding-doubling method |
| $H$ | H function |
| $I$ | radiance |
| $i$ | radiative heat flux in the downward direction in the Kubelka-Munk model |
| $j$ | radiative heat flux in the upward direction in the Kubelka-Munk model |
| $K$ | absorption coefficient in the Kubelka-Munk model |
| $l$ | step size of the movement of a photon bundle |
| $P$ | power |
| $q_{hem}$ | hemispherical radiative heat flux |
| $R$ | reflectance |
| $R_1, R_2, R_3$ | random number |
| $r$ | reflection function in the adding-doubling method |
| $S$ | scattering coefficient in the Kubelka-Munk model or the three flux model |

| | |
|---|---|
| $S_1, S_2$ | scattering coefficients in the three-flux model |
| $s$ | physical distance inside a medium |
| $\hat{\mathbf{s}}$ | direction vector inside a medium |
| $T$ | transmittance |
| $t$ | transmission function in the adding-doubling method |
| $X$ or $Y$ | physical thickness of a medium; Chandrasekar's X or Y function |
| $x$ | coordinate; CIE xy chromaticity; |

Greek Symbols

| | |
|---|---|
| $\alpha$ | absorption coefficient |
| $\beta$ | extinction coefficient |
| $\Theta$ | scattering angle |
| $\theta$ | polar angle |
| $\mu$ | cosine of the polar angle |
| $\xi$ | average path of the radiative heat flux in the Kubelka-Munk model |
| $\sigma$ | scattering coefficient |
| $\sigma'$ | reduced scattering coefficient |
| $\tau$ | optical thickness |
| $\Phi$ | scattering phase function |
| $\phi$ | azimuth angle |
| $\Omega$ | solid angle |
| $\omega$ | single scattering albedo |

Subscripts

| | |
|---|---|
| o | observation |
| i | incidence |
| dif | diffuse |
| col | collimated |
| ref | reflection |
| tran | transmission |
| HG | Heyney-Greenstein |
| KM | Kubelka-Munk |
| hem | hemispherical |

# SUMMARY

The scattering of light in a turbid medium, such as Polytetrafluoroethylene (PTFE), has been studied in various areas including colorimetry, atmosphere science, astrophysics, and photometry. As early as in 1905, Schuster studied the light radiation through a foggy atmosphere, and developed the so-called two-flux method. The Kubelka-Munk model is a very useful particular case of Schuster's theory without considering the spontaneous emission of the diffuse medium. Researchers have added other fluxes to the two-flux approximation, and developed the three-flux method, four-flux method, etc. The angle-resolved scattering of a turbid medium could not be predicted until the more general radiative transfer equation (RTE) was developed. The common techniques for solving the RTE include Chandrasekhar's $X$ and $Y$ functions, discrete-ordinates method, Monte Carlo method, and the adding-doubling method.

PTFE is a highly scattering material and has been regarded to have optical properties similar to biological tissues. While many studies have measured the bidirectional reflectance distribution function (BRDF) of a thick PTFE slab, little is known in regards to its scattering coefficient and scattering phase function. In the present study, the ranges of the scattering coefficient, absorption coefficient, and the asymmetric parameter of the Henyey-Greenstein scattering phase function are assessed using semitransparent sintered PTFE films whose thicknesses range from 0.11 mm to 10 mm. The BRDF and bidirectional transmittance distribution function (BTDF) of these PTFE films were measured using a laser scatterometer at a wavelength of 635 nm, and the

directional-hemispherical reflectance and transmittance were obtained by integrating BRDF and BTDF at normal incidence. In order to minimize the influence of the biased uncertainty of the scatterometer, the ratio of the reflectance and transmittance was fitted with that calculated by the adding-doubling method. The scattering coefficient of PTFE is estimated to exceed 1200 $cm^{-1}$. On the other hand, the absorption coefficient should be less than 0.01 $cm^{-1}$ in order for the directional-hemispherical reflectance of the 10-mm-thick PTFE slab to be near and above 0.98. The ranges of the scattering coefficient and absorption coefficient of PTFE determined in this study differ from that reported in literature.

A Monte Carlo simulation was employed to predict the BRDF and BTDF of PTFE films, then the calculations were compared with measurements at various incidence angles. The accuracy and application regime of some analytical expressions of BRDF and BTDF were also discussed. The approach used in this study is beneficial to the understanding of light scattering in PTFE and other highly scattering media.

# CHAPTER 1

# INTRODUCTION

Light scattering of semi-transparent materials, such as Polytetrafluoroethylene (PTFE), is of great importance in areas including colorimetry, atmosphere science, astrophysics, and photometry. One of the important features of PTFE is its diffuse scattering characteristics. The diffuse reflection of PTFE is mainly due to the volume scattering of light inside the material. When the light enters a PTFE material, it is scattered by microstructures and propagates in random directions before escaping the medium.

While many studies have measured the bidirectional reflectance distribution function (BRDF) of a thick PTFE slab, little is known in regards to its scattering coefficient and scattering phase function. The difficulties of the determination of these parameters are due to the highly scattering characteristics of PTFE. The scattering coefficient can be determined using the Beer's law if the collimated transmittance of a PTFE film with fixed-thickness can be measured. However, unless the PTFE films can be made thinner than approximately four times the mean free path of the incident light, it is difficult to determine the collimated light transmittance. This difficulty also applies to the determination of scattering phase function by measuring the angular distribution of scattered light from a PTFE film because the single scattering condition cannot be guaranteed. Furthermore, the measurement of absorptance of PTFE using an integrating sphere is problematic because the absorption coefficient of this material is so small that

the uncertainty of integrating sphere measurements often makes the absorptance indistinguishable.

In the present study, the ranges of the scattering coefficient, absorption coefficient, and the asymmetric parameter of the Henyey-Greenstein scattering phase function are assessed using semitransparent PTFE films. The BRDF and bidirectional transmittance distribution function (BTDF) of PTFE were measured using a scatterometer. Based on the determined scattering coefficient, absorption coefficient, and asymmetric parameter of the phase function, the BRDF and BTDF are predicted using a Monte Carlo simulation, and compared with the measurements at various incidence angles.

This work involves both instrumentations of optical engineering and mathematical modeling of radiative heat transfer. The work will help people improve the understanding of light scattering in a highly scattering, little absorbing medium, such as PTFE. It is also important for future research of light scattering in biological media for disease diagnostics and laser medicine.

This thesis is organized as follows: Chapter 1 gives an introduction of the project in terms of the problem, approach, and contributions. Chapter 2 presents a literature review in this area. Chapter 3 discusses measurements of the bidirectional and hemispherical properties of PTFE. Chapter 4 describes the theory and results. Chapter 5 draws the conclusions of this study and outlines potential future research.

# CHAPTER 2

# LITERATURE REVIEW

## 2.1 Light Scattering Study of Polytetrafluoroethylene

PTFE has been widely used as diffuse reflectors whose diffuse characteristics are due to the volume scattering of light inside the material. PTFE has been used as the standard of a diffuse reflector for the 200 nm to 2500 nm spectral range by the National Institute of Standards and Technology (NIST) [1]. In remote sensing, PTFE has been used as a calibration standard for onboard sensors on satellites [2-5]. PTFE is used as the coating layer in integrating spheres for the study of reflectance and transmittance of materials [6]. In colorimetry, it is used as whiteness standards [7,8]. The study of the scattering characteristics of PTFE is of great importance.

The light scattering characteristics of PTFE have been studied extensively. In the visible spectrum region, the wavelength and sample density have no obvious influence on the bidirectional properties of PTFE given that the optical thickness of the samples are large [6,9]. The stability of the optical properties of PTFE was tested, and no degradation was apparent following proton bombardment and ultra violet illumination [3]. The degradation of optical properties of a PTFE diffuser after being contaminated by a layer of deposited silicone was modeled [4]. Polarization characteristics of PTFE illuminated by coherent light were studied [10]. Measurement data of the BRDF of PTFE diffusers was published by various research groups [6,7,9,11]. However, few works have

quantitatively compared the measured BRDF data and scattering models of PTFE films at various incident and viewing angles.

## 2.2 Radiative Transfer Equation

The radiative transfer equation (RTE) [12], which governs the radiative heat transfer inside a participating medium, is of great importance in studying light scattering of PTFE. As a beam of light travels a distance $ds$ in a specific direction inside the medium, the radiance is attenuated due to scattering and absorption. Conversely, the radiance is enhanced by blackbody emission and the incoming scattering light from other directions. By considering the change of radiance along a specific direction $\hat{\mathbf{s}}$ due to emission, absorption, scattering away from the radiance (i.e. out-scattering), and scattering into the direction of $\hat{\mathbf{s}}$ (i.e. in-scattering), a general form of RTE is expressed in the following equation.

$$\frac{dI(\hat{\mathbf{s}})}{ds} = \alpha I_b - (\sigma + \alpha) I(\hat{\mathbf{s}}) + \frac{\sigma}{4\pi} \int_{4\pi} I(\hat{\mathbf{s}}_\mathrm{i}) \Phi(\hat{\mathbf{s}}_\mathrm{i}, \hat{\mathbf{s}}) d\Omega_\mathrm{i} \tag{2.1}$$

where $I$ is the radiance, $s$ is the physical distance, $\alpha$ is the absorption coefficient, $\sigma$ is the scattering coefficient, $\hat{\mathbf{s}}_\mathrm{i}$ is the direction vector of the in-scattering radiance, $\Phi$ is the scattering phase function, and $\Omega_\mathrm{i}$ is the solid angle of the in-scattering radiance.

Both directional-hemispherical and bidirectional properties of the medium can be derived by solving the RTE. However, due to the complexity of the equation, there is no effective method to solve the RTE in an analytical format without approximation. In order to solve the RTE researchers developed several numerical methods, including the discrete-ordinates method [13,14], the spherical-harmonics method [15], Mishchenko's

algorithm [16], the finite-element method [17-19], and the Monte Carlo method [20-23], etc. In recent years, the diffusion theory was used to approximate the RTE when the medium is mostly scattering, especially in the field of optical scattering in biological tissues [24-27].

In order to describe the light propagation in a PTFE slab using the RTE, three parameters including the scattering coefficient, absorption coefficient, and the scattering phase function need to be determined. The determination of these parameters typically requires several measurements, among which are [28]: (1) directional-hemispherical reflectance; (2) directional-hemispherical transmittance; (3) absorptance of the sample; (4) collimated light transmittance; and (5) angular distribution of scattered light from a sample whose thickness should be thin enough to guarantee that only single scattering occurs.

Huber et al. [29] reported the three parameters of PTFE by measuring the directional-hemispherical reflectance, directional-hemispherical transmittance, and the collimated light transmittance of samples whose thicknesses ranged from 190 $\mu$m to 845 $\mu$m. The scattering parameters of PTFE reported in their study are very similar to those of biological tissues [28]. For example, the scattering and absorption coefficients at 633 nm were 240 $cm^{-1}$ and 3.6 $cm^{-1}$, respectively. However, it appears that the authors of this study did not distinguish the scattered light in the parallel direction from the collimated light transmission. For PTFE samples with thicknesses greater than 190 $\mu$m, the scattered light would dominate the transmittance even in the direction parallel to the incident light; in other words, the collimated light transmittance is essentially zero and not detectable. Unless the PTFE films can be made thinner than approximately four times the mean free

path of the incident light, it is not feasible to determine the scattering coefficient due to the highly scattering and highly non-isotropic scattering characteristics of a PTFE material. This difficulty also applies to the determination of scattering phase function by measuring the angular distribution of scattered light from a sample because the single scattering condition cannot be guaranteed. Furthermore, the measurement of absorptance of PTFE using an integrating sphere is problematic because the absorption coefficient of this material is so small that the uncertainty of integrating sphere measurements often makes the absorptance indistinguishable.

### 2.3 Modeling of the Directional-Hemispherical Properties

Before the development of the RTE, researchers had studied the directional-hemispherical properties of a turbid medium via several approximation methods. As early as in 1905, Schuster [30] studied the light radiation through a foggy atmosphere, and developed the so-called two-flux method. In color industry, where color matching is of great interest, the Kubelka-Munk model is widely used for the calculation of light reflectance of a turbid medium [31,32]. The Kubelka-Munk model is a very useful particular case of Schuster's theory without considering the spontaneous emission of the diffuse medium [33]. The Kubelka-Munk model has been the most popular method in color-matching industry for more than half century due to its simplicity and effectiveness [33]. Based on the two-flux approximation, researchers developed the three-flux method, four-flux method, etc. [33-37]. Using these approximations, the directional hemispherical properties of a turbid medium can be expressed in closed forms. Comparing with these approximation methods, the adding-doubling method is able to derive the directional-

hemispherical properties by numerically solving the RTE. Due to its effectiveness and accuracy in calculating reflectance and transmittance [38], the adding-doubling method is widely used, especially in the study of light scattering in biological tissues.

### 2.3.1 The Kubelka-Munk model

Originally published in 1931, then with a modification in 1948, the Kubelka-Munk model is widely used nowadays in industries, such as textile, paint, plastics, geophysics, and food, etc., where the calculation of light reflectance of scattering media is needed [31,32]. After the establishment of the Kubelka-Munk model, modifications and some variables trying to address the limitations of the model were proposed. However, the Kubelka-Munk model retained its popularity because of its simplicity. A detailed review and comments of the Kubelka-Munk model and its variables can be found in a review paper [33].

Kubelka and Munk assumed two fluxes of light traveling in a medium, following the treatment originated by Schuster in 1905 when he studied light scattering in a foggy atmosphere. Of these two fluxes of light, one flux travels upward, the other travels downward. The reflectance of the medium can be derived as a simple function of the ratio of the Kubelka-Munk absorption and scattering coefficients. Here, the Kubelka-Munk theory is summarized with some clarifications.

In the 1931 paper, the two fluxes were expressed as $i$ and $j$ as shown in Fig. 2.1 [32]. While passing through an infinitesimal slab of thickness $dx$ from $x_1$ to $x_2$, the intensity changes of the two fluxes are $di$ and $dj$, respectively. A system of differential equations that governs these changes can be derived as Eq. (2.2).

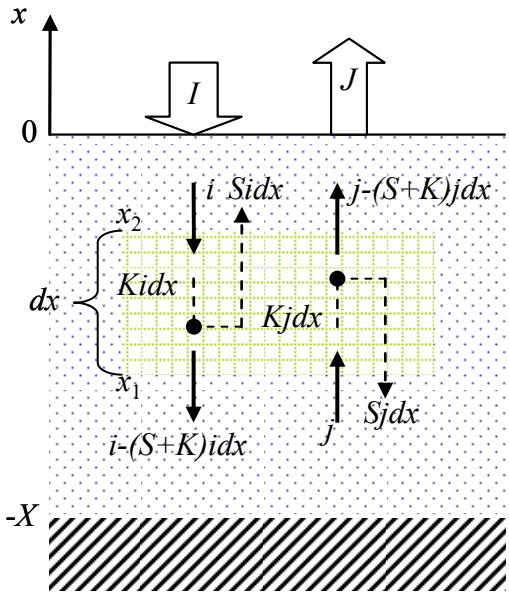


Figure 2.1 Schematic of the two fluxes in the Kubelka-Munk model. Here, *i* represents the downward flux, and *j* represents the upward flux.

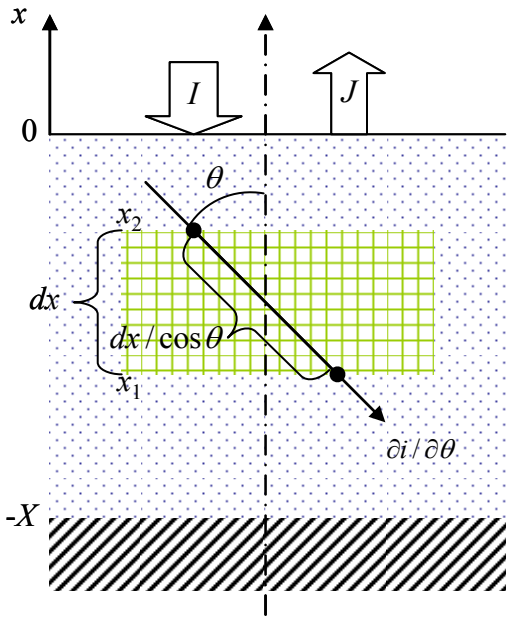


Figure 2.2 The passage of light in Kubelka-Munk's modified model. The angular distribution of light intensity was considered.

$$\begin{aligned} -di &= -(S+K)idx + Sjdx \\ dj &= -(S+K)jdx + Sidx \end{aligned} \tag{2.2}$$

where $S$ is the scattering coefficient; $K$ is the absorption coefficient. After a few steps of derivations, one would obtain the reflectance of a scattering medium with thickness $X$ as

$$R = \frac{\frac{1}{R_\infty}(R_g - R_\infty) - R_\infty(R_g - \frac{1}{R_\infty})e^{-SX(\frac{1}{R_\infty} - R_\infty)}}{(R_g - H_\infty) - (R_g - \frac{1}{R_\infty})e^{-SX(\frac{1}{R_\infty} - R_\infty)}} \tag{2.3}$$

where $R_\infty$ is the reflectance of an infinite scattering layer, and $R_g$ is the reflectance of the substrate layer. Furthermore, $R_\infty$ is a function of the ratio of the absorption coefficient and the scattering coefficient.

$$R_\infty = 1 + \frac{K}{S} - \sqrt{\frac{K^2}{S^2} + 2\frac{K}{S}} \tag{2.4}$$

In his 1948 paper, Kubelka realized the fact that the path of a ray of light passing through a layer of thickness $dx$ is not $dx$ but $dx/\cos\theta$, illustrated in Fig. 2.2 [31]. In other words, the angular distribution of light intensity was considered in this modified model. The average path $d\xi_i$ of the light passing through $dx$ was given as

$$d\xi_i = dx\int_0^{\pi/2} \frac{\partial i}{i\partial\theta}\frac{d\theta}{\cos\theta} = udx = 2dx \tag{2.5}$$

where $\partial i/\partial\theta = i\sin(2\theta)$ is the angular distribution of the light intensity.

However, Kubelka's expression of the average path is somewhat problematic. The physical meaning of $i$ is confusing. The expression of $\partial i/\partial\theta = i\sin(2\theta)$ is not mathematically rigorous. Actually the so-called intensity $i$ in the Kubelka-Munk theory could be considered as the hemispherical radiative heat flux, which is in linear relationship with the diffused light radiance.

$$q_{\text{hem}} = 2\pi \int_0^{\pi/2} I \cos\theta \sin\theta d\theta = \pi I \tag{2.6}$$

where $I$, with unit W/(m$^2$sr), is the radiance inside the medium. Since the scattering of light inside the medium is assumed isotropic in Kubelka-Munk's theory, $I$ does not depend on $\theta$. The relationship of $\partial i / \partial \theta = i \sin(2\theta)$ should be understood as the angular distribution of heat flux, or the contribution of the amount of heat flux within an infinitesimal polar angle $d\theta$ to the hemispherical heat flux

$$\frac{dq(\theta)}{d\theta} = 2\pi I \cos\theta \sin\theta = \pi I \sin(2\theta) = q_{\text{hem}} \sin(2\theta) \tag{2.7}$$

An alternative method is to directly calculate the weighted average of $\frac{dx}{\cos\theta}$ over the hemispherical range using the following equation:

$$\begin{aligned} d\xi_{\text{i}} &= \left\langle \frac{dx}{\cos\theta} \right\rangle = \frac{\int_0^{2\pi} \int_0^{\pi/2} \frac{dx}{\cos\theta} I \cos\theta \sin\theta d\theta d\phi}{\int_0^{2\pi} \int_0^{\pi/2} I \cos\theta \sin\theta d\theta d\phi} \\ &= dx \int_0^{\pi/2} \frac{2\pi I \sin\theta d\theta}{q_{\text{hem}}} \end{aligned} \tag{2.8}$$

Therefore,

$$u = \int_0^{\pi/2} \frac{2\pi I \sin\theta d\theta}{q_{\text{hem}}} \tag{2.9}$$

For diffused light, $u = 2$ since $I$ does not depend on $\theta$. With the modification of the light path from $dx$ to $d\xi_{\text{i}}$, the reflectance was derived as the following expression.

$$R = \frac{1 - R_{\text{g}}\left[a - b \cdot \coth(bSX)\right]}{a + b \cdot \coth(bSX) - R_{\text{g}}} \tag{2.10}$$

where $a = (S + K)/S$, $b = \sqrt{a^2 - 1}$, $S$ and $K$ are the Kubelka-Munk scattering and absorption coefficients, and $R_{\text{g}}$ is the reflectance of the substrate layer.

The Kubelka-Munk model has been widely used in industry for the calculation of hemispherical reflectance of a turbid medium due to its simplicity. However, the applications of the model were limited by its assumptions. The Kubelka-Munk model cannot deal with parallel light. To address the issue of directional light, the three-flux and four-flux models were proposed.

### 2.3.2 Three-flux model

The three-flux model [13,39,40] is used to predict the reflectance and transmittance of a turbid medium with a collimated incidence of light. In this model, there are three fluxes in the medium as shown in Fig. 2.3. Here, $F_1$ represents the collimated beam traveling in the positive $x$ direction, $F_2$ represents the diffuse flux in the same direction of $F_1$, and $F_3$ represents the diffuse flux in the opposite direction of $F_2$. Within a differential distance $dx$, the collimated flux can be scattered into the diffuse fluxes $F_2$ and $F_3$. The diffuse fluxes $F_2$ and $F_3$ can be scattered into each other. However the diffuse fluxes $F_2$ and $F_3$ cannot be scattered into $F_1$ since there is no solid angle associated with $F_1$ due to its collimation characteristics. The governing equations are given as [13,40]

$$\frac{dF_1}{dx} = -(a + S_1 + S_2)F_1 \tag{2.11}$$

$$\frac{dF_2}{dx} = S_1F_1 - (A + S)F_2 + SF_3 \tag{2.12}$$

$$-\frac{dF_3}{dx} = S_2F_1 + SF_2 - (A + S)F_3 \tag{2.13}$$

where $a$ is the absorption coefficient of the collimated flux $F_1$, $A$ is the absorption coefficient of the diffuse fluxes of $F_2$ and $F_3$, $S_1$ is the scattering coefficient from the collimated flux $F_1$ to the diffuse flux $F_2$, $S_2$ is the scattering coefficient from the collimated flux $F_1$ to the diffuse flux $F_3$, $S$ is the scattering coefficient from a diffuse flux to the diffuse flux of the opposite direction. It is noted that the absorption coefficient $a$ in the three-flux model equals $\alpha$ which is the absorption coefficient used in the RTE. Solutions of the above system of equations are

$$F_1 = C_1 e^{-mx} \tag{2.14}$$

$$F_2 = C_1 e^{-mx} + C_2(1+G)e^{-\nu x} + C_3(1-G)e^{\nu x} \tag{2.15}$$

$$F_3 = C_1 e^{-mx} + C_2(1-G)e^{-\nu x} + C_3(1+G)e^{\nu x} \tag{2.16}$$

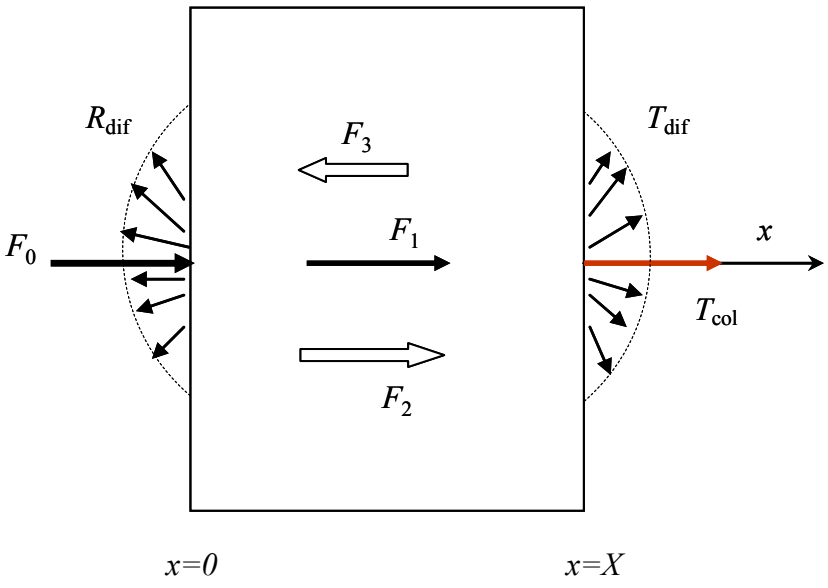


Figure 2.3 Illustration of the three-flux method for the study of light scattering and absorption in a turbid medium. $F_0$ represents the collimated incidence beam. $F_1$ represents the collimated beam traveling in the positive $x$ direction. $F_2$ represents the diffuse flux in the same direction of $F_1$. $F_3$ represents the diffuse flux in the opposite direction of $F_2$.

where $m = a + S_1 + S_2$, $\nu = \left[A(A+2S)\right]^{1/2}$, and $G = \left[A/(A+2S)\right]^{1/2}$. The diffuse reflectance diffuse transmittance and collimated light transmittance are: $R_{\text{dif}} = F_3(0) - F_2(0)$, $T_{\text{dif}} = F_2(X) - F_3(X)$, and $T_{\text{col}} = F_1(X)$.

In this study, the PTFE films were illuminated by collimated light flux $F_0$. If $F_0 = 1$, then the unscattered transmittance, the total transmittance, and the total reflectance are $F_1(X)$, $F_2(X)$, and $F_3(0)$, respectively. The system is subjected to these boundary conditions: $F_1(0) = F_0 = 1$, $F_2(0) = 0$, and $F_3(X) = 0$. Therefore,

$$C_1 = 1 \tag{2.17}$$

$$C_3 = \frac{B_2(1+G)e^{-mX} - B_1(1-G)e^{-\nu X}}{(1-G)^2 e^{-\nu X} - (1+G)^2 e^{\nu X}} \tag{2.18}$$

$$C_2 = -\frac{C_3(1-G) + B_1}{1+G} \tag{2.19}$$

where $B_1 = \frac{SS_2 + (A+S+m)S_1}{\nu^2 - m^2}$, and $B_2 = \frac{SS_1 + (A+S-m)S_2}{\nu^2 - m^2}$. The values of the five parameters, $a$, $A$, $S$, $S_1$, and $S_2$ of the three-flux model depend on material properties. It is known that the summation of $S_1$ and $S_2$ equals the scattering coefficient used in RTE [13]

$$\sigma = S_1 + S_2 \tag{2.20}$$

Furthermore, $S_1$ correlates with $\sigma$ and the scattering phase function as indicated in the following functions.

$$\begin{aligned} S_1 &= \frac{\sigma}{2}\left(1 + \sum_{i=1,3,5\ldots}^{\infty} g_i (-1)^{(i-1)/2} \frac{(1\cdot 3\cdot 5\ldots i)^2}{i(i+1)i!}\right) \\ &= \frac{\sigma}{2}\left(1 + \frac{g_1}{2} - \frac{g_3}{8} + \frac{g_5}{16} - \frac{5g_7}{128} + \frac{7g_9}{256}\ldots\right) \end{aligned} \tag{2.21}$$

$$g_n = (n + \frac{1}{2}) \int_{-1}^{+1} \Phi(\cos\Theta) P_n(\cos\Theta) d(\cos\Theta) \tag{2.22}$$

where the scattering angle $\Theta$ is angle between the propagation direction of a photon bundle before a scattering event and that after a scattering event, $\Phi$ is the scattering phase function, and $P_n$ is the Legendre polynomial. Furthermore, it is found that $A \approx 2\alpha$ and $S \approx \sigma(3g_0 - g_1)/4$ [13]. Here, $\alpha$ and $\sigma$ are the absorption and scattering coefficients used in RTE, respectively.

The three-flux model has been used for the modeling of light propagation in a gray epoxy paint [39], where the relationship between $S_1$ and $\sigma$ described in Eq. (2.21) was simplified as $S_1 = \sigma(1 + g_1/2)/2$. All the higher order terms were neglected. It is noted that this simplification is only valid for materials whose average cosine of the scattering phase function (i.e. the asymmetric parameter, *g*) is small. On the other hand, this simplification could introduce large errors if the materials to be modeled are highly anisotropic. Therefore, the higher the degree of anisotropic scattering of the sample, the more terms should be used in Eq. (2.21) in order to minimize the error caused by the truncation of higher order terms.

### 2.3.3 Adding-Doubling method

The adding-doubling method was introduced by van de Hulst [41] to solve the RTE in a parallel slab composed of multiple layers. In the adding method, if the reflection and transmission functions of each individual layer are known, the reflection and transmission functions of the composite can be calculated. The adding method is termed as the doubling method when the layers are identical in both thickness and all the

RTE parameters [42]. The reflection and transmission functions for an arbitrarily thick slab can be obtained by repeatedly adding and doubling the layers until the desired thickness is reached. Subsequently, the directional-hemispherical reflectance and transmittance can be calculated by integrating the reflection and transmission functions. The adding-doubling method requires the knowledge of the scattering albedo, optical thickness $\tau = (\sigma + \alpha)d$ with $d$ as the film thickness, and the asymmetric parameter of the scattering phase function to predict the directional-hemispherical properties of PTFE films.

At the first step, the adding-doubling method numerically solves the RTE for a starting thin slab of the medium. For example, the starting thin slab could be so thin that only single scattering happens in the slab. For such a thin layer, the single scattering reflection function can be defined as [43]

$$r(\omega, \tau, \mu, \mu_i) = \frac{\omega \pi h(\mu, -\mu_i)}{\mu + \mu_i} \left[ 1 - \exp\left( -\frac{\tau}{\mu} - \frac{\tau}{\mu_i} \right) \right] \tag{2.23}$$

where $\omega$ is the single scattering albedo, $h$ is the scattering redistribution function, $\tau$ is the optical thickness, $\mu_i$ is the cosine of the incidence polar angle, and $\mu$ is the cosine of the reflected radiance polar angle. For Henyey-Greenstein scattering function, the redistribution function can be expressed as [43]

$$h(\mu, \mu_i) = \frac{2}{\pi} \frac{1 - g^2}{\sqrt{M + N}\,(M - N)} E(U) \tag{2.24}$$

where $g$ is the asymeteric parameter (average cosine) of the Henyey-Greenstein phase function, and the parameters of $M$, $N$, and $U$ are defined as $M = 1 + g^2 - 2g\mu\mu_i$, $N = 2g\sqrt{1-\mu^2}\sqrt{1-\mu_i^2}$, $U = \sqrt{2\gamma/(\alpha+\gamma)}$, and $E(U)$ is the complete elliptical integral

[43]. The internal reflection and boundary conditions could also be considered if applicable. The single scattering transmission function for thin layer is [43]

$$t(\omega,\tau,\mu,\mu_{\mathrm{i}})=\begin{cases}\dfrac{\omega\pi h(\mu,-\mu_{\mathrm{i}})}{\mu_{\mathrm{i}}-\mu}\left[\exp\left(-\dfrac{\tau}{\mu_{\mathrm{i}}}\right)-\exp\left(-\dfrac{\tau}{\mu}\right)\right] & \text{if} \quad \mu_{\mathrm{i}}\neq\mu \\ \dfrac{\omega\pi h(\mu,-\mu_{\mathrm{i}})}{\mu_{\mathrm{i}}-\mu}\exp\left(-\dfrac{\tau}{\mu_{\mathrm{i}}}\right)+\dfrac{1}{2u}\exp\left(-\dfrac{\tau}{\mu}\right) & \text{if} \quad \mu_{\mathrm{i}}=\mu\end{cases} \tag{2.25}$$

The reflection function and the transmission function are used to transform any incident radiance distribution $I_{\mathrm{in}}(\mu_{\mathrm{i}})$ into the reflected radiance distribution $I_{\mathrm{ref}}(\mu)$ and transmitted radiance distribution $I_{\mathrm{tran}}(\mu)$ by [41]

$$I_{\mathrm{ref}}(\mu)=\int_0^1 r(\mu,\mu_{\mathrm{i}})I_{\mathrm{in}}(\mu_{\mathrm{i}})2\mu_{\mathrm{i}}d\mu_{\mathrm{i}} \tag{2.26}$$

$$I_{\mathrm{tran}}(\mu)=\int_0^1 t(\mu,\mu_{\mathrm{i}})I_{\mathrm{in}}(\mu_{\mathrm{i}})2\mu_{\mathrm{i}}d\mu_{\mathrm{i}} \tag{2.27}$$

With the knowledge of $I_{\mathrm{ref}}(\mu)$ and $I_{\mathrm{tran}}(\mu)$, the directional-hemispherical reflectance and transmittance can be calculated by integration.

The adding-doubling method can also be used inversely, and called the Inverse Adding Doubling (IAD) method. With the knowledge of the reflectance and transmittance of the starting thin slab, the IAD method uses the following steps to determine the optical properties of the medium [42]: (1) Guess a set of initial values of the optical properties to be determined; (2) Calculate the reflectance and transmittance of the sample using the adding-doubling method based on the guessed initial values and the reflectance and transmittance of the starting thin slab; (3) Compare the calculated reflectance and transmittance with the measured ones, and find out the error which defines how far the calculated values are from the measured reflectance and

transmittance; and (4) Adjust the initial set of parameters based on the error between the calculation and the measurement, then repeat the calculation until a match is made.

## 2.4 Modeling of the Bidirectional Properties

The angle-resolved scattering of a turbid medium could not be predicted until the more general RTE was developed and able to be solved [12]. Besides the numerical solutions, such as the discrete-ordinates method and the Monte Carlo method, some approximate analytical expressions are able to describe the bidirectional reflectance of a turbid medium in closed forms for some special cases [44-51]. Some of these closed forms, including the Hapke's model, the Pierce-Marcus formulae, and the Sobolev-Kokhanovsky model, will be discussed in this section.

### 2.4.1 Terminologies related with bidirectional properties

Although BRDF is the most basic of all radiation properties, the original forms of these models do not follow a unified expression such as the BRDF to describe the bidirectional properties. The definitions of these different expressions of bidirectional properties are given in this section. Their relationships with the BRDF are also discussed.

The BRDF is defined as the reflected radiance divided by the incident irradiance [52], and given as

$$f_r = \frac{dI_{\mathrm{r}}}{dP_{\mathrm{i}}} = \frac{dI_{\mathrm{r}}}{I_{\mathrm{i}} \cos\theta_{\mathrm{i}} d\Omega_{\mathrm{i}}} \tag{2.28}$$

where $I_r$ is the reflected radiance, $P_i$ is the incident irradiance, $I_i$ is the incident radiance, $\theta_i$ is the polar angle of the incident light, and $\Omega_i$ is the solid angle of the incident light. For collimated light, the incident energy flux can be calculated as

$$\pi F = \int_{2\pi} I_i \delta(\Omega_i - 0) \cos\theta_i d\Omega_i = I_i \cos\theta_i = P_i \tag{2.29}$$

where $F$ describes how much the reflected radiance would be if the medium is a Lambertian diffuser and the incident power is evenly reflected in all the directions perfectly.

The radiance factor [53] is defined as $\rho = I_r / (F \cos\theta_i)$. Therefore, the relationship between radiance factor and the BRDF is given as:

$$\rho = \frac{I_r}{F \cos\theta_i} = \frac{f_r P_i}{(1/\pi) P_i \cos\theta_i} = \frac{\pi f_r}{\cos\theta_i} \tag{2.30}$$

Hapke [44] defined the bidirectional reflectance as the ratio of the reflected radiance and the incident radiance $\chi = I_r / I_i$. Since $I_i \cos\theta_i = P_i$ for collimated incident light according to Eq. (2.29), the relationship between $\chi$ amd $f_r$ is given as

$$\chi = f_r \cos\theta_i \tag{2.31}$$

In the following sections, different expressions of bidirectional properties in these models will be converted to the BRDF whenever practical.

### 2.4.2 Hapke's model

Based on the RTE, Hapke derived approximate analytic expressions of the bidirectional properties of a scattering medium [44]. The medium can be of arbitrary single-scattering albedo and phase function. The limitation is that the optical thickness of the medium should be infinite. In the coordinate system used by Hapke, the plane surface

at $z = 0$ separates an empty half space $z > 0$ from a half space $z < 0$ containing the scattering medium. The incident collimated light of intensity $I_{\mathrm{i}}$ travels into a direction which forms an angle $\pi - \theta_{\mathrm{i}}$ with the upward *z*-axis and has an azimuth angle $\phi = 0$. The reflected light forms a zenith angle of $\theta$ with the *z*-axis.

Hapke handled the problem by separating the radiance into a singly scattered radiance and a multiply scattered radiance. The former can be calculated exactly for any arbitrary phase function. The later was calculated using the Schuster two-flux approximation, in which the isotropic scattering assumption was assumed based on the reasoning that the directional effect would be averaged out in a semi-infinite medium. Therefore, the model is referred to as the isotropic multiple-scattering approximation (IMSA).

Hapke started with the light scattering inside of a volume element $dV = L^2 d\Omega dL$, where *L* is the distance between the volume and the detector, and $\Omega$ is the solid angle of the volume element. The incident light of the volume *dV* is separated into two parts. The first part, $I'$, is the radiance that comes from the collimated incident light and is exponentially attenuated by the passage from the surface to the volume *dV*. The other part, $I''$, is the diffuse light which has been scattered one or more times by other particles before striking on the volume. The power scattered by the particles in *dV* toward the detector can be expressed as

$$dP = \frac{\omega}{4\pi}\left\{\int_{4\pi}\left[I'(z,\Omega') + I''(z,\Omega')\right]\Phi(\Omega',\Omega)d\Omega'\right\}\beta dV\frac{dA}{L^2} \tag{2.32}$$

where $\omega$ is the single scattering albedo, $\beta = \sigma + \alpha$ is the extinction coefficient, and $\Phi$ is the phase function. The radiance pointing from the volume element towards the detector is

$$dI = \frac{dP}{dA d\Omega} = \frac{\omega}{4\pi}\left\{\int_{4\pi}\left[I'(z,\Omega') + I''(z,\Omega')\right]\Phi(\Omega',\Omega)d\Omega'\right\}\beta dL \tag{2.33}$$

Along the passage of the volume and the detector, which is located at $L_0$, the light is attenuated by a factor of $e^{-\beta(L-L_0)} = e^{\beta z/\mu} = e^{-\beta\tau}$, where $\mu = \cos\theta$. The singly scattered radiance is given as

$$I_S = \frac{\omega}{4\pi}\int_{-\infty}^{0}\left[\int_{4\pi} I'(z,\Omega')\Phi(\Omega',\Omega)d\Omega'\right] e^{\beta z/\mu}\frac{\beta}{\mu}dz \tag{2.34}$$

where $I' = I_i e^{-\beta z/\cos(\pi-\theta_i)}\delta\left[\theta-(\pi-\theta_i)\right]\delta(\phi-0)$ with $\delta$ as the Dirac-delta function and $I_i$ as the radiance of the incident light, $z$ is the distance from the volume to the surface of the medium, and $\mu = \cos\theta$. Therefore, the singly scattered radiance reaching the detector can be calculated exactly.

$$\begin{aligned} I_S &= \frac{\omega}{4\pi}\int_{-\infty}^{0}\left[\int_{4\pi} I_i e^{-\beta z/\cos(\pi-\theta_i)}\delta\left[\theta-(\pi-\theta_i)\right]\delta(\phi-0)\Phi(\Omega',\Omega)d\Omega'\right] e^{\beta z/\mu}\frac{\beta}{\mu}dz \\ &= \frac{\omega}{4\pi}\int_{-\infty}^{0} I_i \exp\left[\beta z\left(\frac{1}{\mu_i}+\frac{1}{\mu}\right)\right]\Phi(\Omega',\Omega)\frac{\beta}{\mu}dz = I_i\frac{\omega}{4\pi}\frac{\mu_i}{\mu_i+\mu}\Phi(\Omega',\Omega) \end{aligned} \tag{2.35}$$

where $\mu_i = \cos\theta_i$. The multiply scattered radiance can be expressed as

$$I_M = \frac{\omega}{4\pi}\int_{-\infty}^{0}\left[\int_{4\pi} I''(z,\Omega')\Phi(\Omega',\Omega)d\Omega'\right] e^{\beta z/\mu}\frac{\beta}{\mu}dz \tag{2.36}$$

The radiance reaching the detector is the summation of the singly scattered radiance and the multiply scattered radiance.

$$I = I_S + I_M \tag{2.37}$$

To evaluate $I_M$, the two-flux approximation for isotropic scattering was used on the RTE. It turns out that the multiply scattered radiance can be approximated as

$$I_M = I_i \frac{\omega}{4\pi} \frac{\mu_i}{\mu_i + \mu} \left[ H(\mu_i) H(\mu) - 1 \right] \tag{2.38}$$

where $H(\mu) = \frac{1 + 2\mu}{1 + 2\mu\sqrt{1-\omega}}$. Therefore, the Hapke model explicitly expresses the BRDF in the following closed-form equation.

$$f_r = \frac{\omega}{4\pi} \frac{1}{\mu_i + \mu} \left[ \Phi(\Omega', \Omega) + H(\mu_i) H(\mu) - 1 \right] \tag{2.39}$$

Comparing with numerical solutions of RTE, some researchers complained its low accuracy, violation of the energy conservation law, and ability to produce unphysical results [16]. Nevertheless, the closed-form expression bears physical meanings by explicitly containing some physical quantities. If the requirement of the absolute accuracy of the applications is not high, or if the assumptions or the approximations of some parameters of the system limit the accuracy of the system, the exact numerical solutions are no more useful, and much more involved, than the closed-form formula.

### 2.4.3 The Pierce-Marcus formulae

Comparing with the Hapke model, the limitation of the scattering to be semi-infinite is released in Pierce and Marcus's formulae. The drawback of Pierce and Marcus's expressions is that the scattering phase function of the medium has to be isotropic. The coordinate system used by Pierce and Marcus is similar as the one used by Hapke. The plane $z = 0$ separates the space and the scattering medium. The *z*-axis points

upwards to the space. The direction of the incident light forms an angle of $\pi - \theta_{\mathrm{i}}$ with the *z*-axis. The direction of the reflected light forms an angle $\theta$ with the *z*-axis.

Pierce and Marcus started with the expression of BRDF of an isotropic medium in terms of Chandrasekar's *X* function and *Y* function [53].

$$f_{\mathrm{r}} = \frac{\omega}{4\pi}\frac{1}{\mu + \mu_{\mathrm{i}}}\left[X(\mu)X(\mu_{\mathrm{i}}) - Y(\mu)Y(\mu_{\mathrm{i}})\right] \tag{2.40}$$

where $\mu_{\mathrm{i}} = \cos\theta_{\mathrm{i}}$, $\mu = \cos\theta$, and $\omega$ is the single scattering albedo. The major contribution of Pierce and Marcus was the development of the approximate formulae to calculate both the *X* and *Y* functions, so as to express the BRDF explicitly. Pierce and Marcus also employed the two-flux approximation method, which converts the RTE into a system of differential equations of the upwards flux and downwards flux. The *X* and *Y* functions were able to be approximated with the facility of the system of differential equations and its boundary conditions.

$$\begin{aligned} X(\mu) = {} & \frac{(1+2\mu)}{(1-\gamma^2\mu^2)} - \frac{\gamma\mu}{(1-\gamma^2\mu^2)} \\ & \times\left[\frac{D(1+2\mu) + 2(2+\gamma)\times(2-\gamma)(1-2\mu)e^{-\tau/\mu}}{(2+\gamma)^2 e^{\gamma\tau} - (2-\gamma)^2 e^{-\gamma\tau}}\right] \end{aligned} \tag{2.41}$$

$$\begin{aligned} Y(\mu) = {} & \frac{(1-2\mu)e^{-\tau/\mu}}{(1-\gamma^2\mu^2)} + \frac{\gamma\mu}{(1-\gamma^2\mu^2)} \\ & \times\left[\frac{2(2+\gamma)(2-\gamma)(1+2\mu) + D(1-2\mu)e^{-\tau/\mu}}{(2+\gamma)^2 e^{\gamma\tau} - (2-\gamma)^2 e^{-\gamma\tau}}\right] \end{aligned} \tag{2.42}$$

where $\gamma = 2\sqrt{1-\omega}$, $\tau$ is the optical thickness, and $D = (2+\gamma)^2 e^{\gamma\tau} + (2-\gamma)^2 e^{-\gamma\tau}$. When the optical thickness goes to infinity, the *Y* function goes to zero, and the *X* function reduces to the *H* function that is of the same expression as in the Hapke model. The BRDF then reduces to

$$f_r = \frac{\omega}{4\pi}\frac{H(\mu)H(\mu_i)}{\mu+\mu_i} \tag{2.43}$$

Therefore, in the case of isotropic and semi-infinite medium, the expression of BRDF is the same as that of the Hapke model

### 2.4.4 The Sobolev-Kokhanovsky model

Figure 2.4 illustrates the coordinate system used in the Sobolev model. The *z*-axis directs downward, and is perpendicular to the boundary of the medium. The polar angle $\theta$ denotes the angle between the downward *z*-axis and the radiance vector of interest. The azimuth angle $\phi$ of a radiance vector is measured from the *x*-axis in the clockwise direction when looking upward. The azimuth angle of the incident radiation is assumed to be zero. It is also defined that $\eta = \cos\theta$, $\mu = |\eta|$, $\xi = \cos\theta_i$, and $\mu_i = |\xi|$.

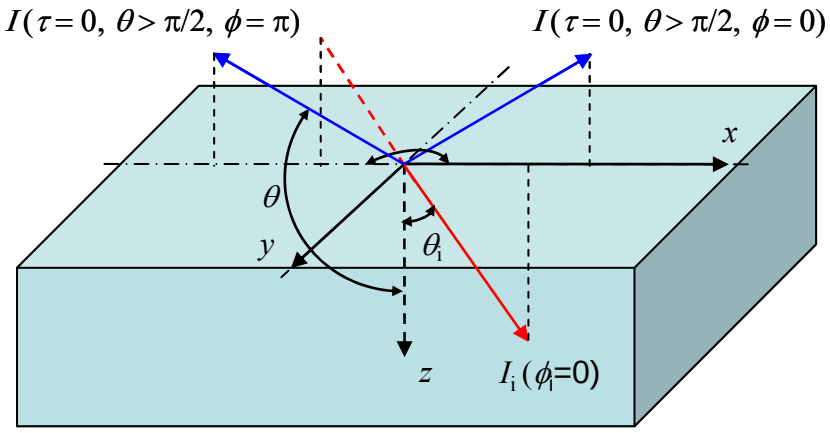


Figure 2.4 The coordinate system used in the Sobolev model. One incident light beam and two reflected light beams from the top of the scattering layer are illustrated. It is noted that two reflected beams of light have azimuth of 0 and π, respectively. The zenith angle of the reflected radiation falls between π/2 and π.

Based on the RTE, but in a particular way, Sobolev derived the reflectance of a scattering medium at large optical thickness [50,51]. This method was reviewed in detail by Kokhanovsky [48]. Rather than using the two-flux method in solving the RTE as in the Hapke model and Pierce and Marcus's model, Sobolev started by assuming that the radiance at large optical thickness can be expressed as:

$$I(\tau,\eta) = i(\eta)e^{-k\tau} \tag{2.44}$$

where $k$ is the diffusion exponent, and the function $i(\eta)$ describes the angular distribution of light intensity in deep layers of semi-infinite scattering media. Following the RTE, the function $i(\eta)$ is defined as

$$i(\eta) = \frac{\omega}{2(1-k\eta)}\int_{-1}^{1}\Phi(\eta,\eta')i(\eta')d\eta' \tag{2.45}$$

The bidirectional reflection and transmission function is defined as $R(\eta,\xi,\tau_0) = I(-\eta,\xi,0)/\left[I_{\mathrm{i}}(\eta,\xi,0)\xi\right]$ and $T(\eta,\xi,\tau_0) = I(\eta,\xi,\tau_0)/I_{\mathrm{i}}(\eta,\xi,0)$. Here, $I_{\mathrm{i}}$ is defined such that $\pi I_{\mathrm{i}}$ is the net flux per unit area normal to the incident light beam, and $\tau_0$ is the optical thickness of the whole scattering medium. From the physical grounds and symmetry relations of reflectance $R(\eta,\xi,\tau_0)$ and transmittance $T(\eta,\xi,\tau_0)$, Sobolev made another assumption as the following equations.

$$R(\eta,\xi,\tau_0) = R_\infty(\eta,\xi) - f(\tau_0)K(\eta)K(\xi) \tag{2.46}$$

$$T(\eta,\xi,\tau_0) = g(\tau_0)K(\eta)K(\xi) \tag{2.47}$$

where $R_\infty(\eta,\xi) \equiv R(\eta,\xi,\tau_0=\infty)$, and $K(\eta)$ is the intensity of escaped radiation in Mulne's problem (i.e. for radiation sources at infinite optical depth).

Based on these two assumptions and the RTE, Sobolev was able to derive the following relationships.

$$R(\eta,\xi,\tau_0) = R_\infty(\eta,\xi) - T(\eta,\xi,\tau_0) l e^{-k\tau_0} \tag{2.48}$$

$$T(\eta,\xi,\tau_0) = tK(\eta)K(\xi) \tag{2.49}$$

where $t = \dfrac{me^{-k\tau_0}}{1-l^2e^{-2k\tau_0}}$, $K(\mu) = \dfrac{i(\mu)}{m} - \dfrac{2}{m}\int_0^1 R_\infty(\mu,\mu_\mathrm{i}) i(-\mu_\mathrm{i})\mu_\mathrm{i} d\mu_\mathrm{i}$,

$i(\eta) = \dfrac{\omega}{2(1-k\eta)}\int_{-1}^{1}\Phi(\eta,\eta')i(\eta')d\eta'$, and $R_\infty$ is the Ambarzumian integral equation which is expressed as [50]

$$\begin{aligned} R_\infty(\mu_\mathrm{i},\phi_\mathrm{i},\mu,\phi) = {} & \frac{\omega}{4(\mu+\mu_\mathrm{i})}\Phi(\theta) \\ & + \frac{\mu_0\omega}{4\pi(\mu+\mu_\mathrm{i})}\int_0^1\int_0^{2\pi}\Phi(\mu,\phi,\mu',\phi')R_\infty(\mu',\phi',\mu_\mathrm{i},\phi_\mathrm{i})d\mu' d\phi' \\ & + \frac{\mu\omega}{4\pi(\mu+\mu_\mathrm{i})}\int_0^1\int_0^{2\pi}\Phi(\mu_\mathrm{i},\phi_\mathrm{i},\mu',\phi')R_\infty(\mu',\phi',\mu,\phi)d\mu' d\phi' \\ & + \frac{\omega\mu\mu_\mathrm{i}}{4\pi^2(\mu+\mu_\mathrm{i})}\int_0^1 d\phi'\int_0^{2\pi}R_\infty(\mu',\phi',\mu,\phi)d\mu' \\ & \times\int_0^{2\pi}d\phi''\int_0^1\Phi(-\mu',\phi',\mu'',\phi'')R_\infty(\mu'',\phi'',\mu_\mathrm{i},\phi_\mathrm{i})d\mu'' \end{aligned} \tag{2.50}$$

For some particular cases, closed-form approximation formulae were derived from these relationships.

For isotropic scattering medium, Eqs. (47) and (48) are reduced to

$$R(\tau_0,\mu,\mu_\mathrm{i}) = \frac{\omega H(\mu)H(\mu_\mathrm{i})}{4(\mu+\mu_\mathrm{i})} - \frac{T(\tau_0,\mu,\mu_\mathrm{i})ma_0^2\omega e^{-k\tau_0}}{2k} \tag{2.51}$$

$$T(\tau_0,\mu,\mu_\mathrm{i}) = t\left(\frac{\omega_0 a_0}{2}\right)^2\frac{H(\mu)H(\mu_\mathrm{i})}{(1-k\mu)(1-k\mu_\mathrm{i})} \tag{2.52}$$

where $t = \frac{me^{-k\tau_0}}{1-l^2e^{-2k\tau_0}}$, $m = \frac{4}{k}\left(\frac{1}{1-k^2} - \frac{1}{\omega_0}\right)$, $l = \frac{ma_0^2\omega}{2k}$, $a_0 = \frac{2k}{m}\int_0^1 \frac{H(\mu)}{1-k^2\mu^2}\mu d\mu$, and $\frac{1}{2k}\ln\left(\frac{1+k}{1-k}\right) = \frac{1}{\omega}$. As the optical thickness goes to infinity, the reflectance factor becomes the Hapke model in the case of isotropic scattering.

Furthermore, if the medium is non-absorbing, it follows from Eqs. (2.51) and (2.52) that

$$R(\tau_0, \mu, \mu_i, \phi) = R_\infty^0(\mu, \mu_i, \phi) - T(\tau_0, \mu, \mu_i) \tag{2.53}$$

$$T(\tau_0, \mu, \mu_i) = \frac{K_0(\mu)K_0(\mu_i)}{0.75(1-g)\tau_0 + \Delta} \tag{2.54}$$

where $R_\infty^0$ is the function of $R_\infty$ at $\omega = 1$, $\Delta = 3\int_0^1 K_0(\mu)\mu^2 d\mu$, $K_0(\mu)$ can be approximated by $K_0(\mu) \approx \frac{3}{7}(1+2\mu)$, and $g$ is the asymmetric parameter of the Heney-Greenstein phase function defined as

$$\Phi(\Theta) = \frac{1-g^2}{\left(1+g^2-2g\cos\Theta\right)^{3/2}} \tag{2.55}$$

where the scattering angle $\Theta$ is angle between the propagation direction of a photon bundle before a scattering event and that after a scattering event. The scattering angle can be calculated by the zenith and azimuth angles of the light using

$$\cos\Theta = \cos\theta\cos\theta_i + \sin\theta\sin\theta_i\cos(\phi - \phi_i) \tag{2.56}$$

It follows that

$$\Delta = 3\int_0^1 \frac{3}{7}(1+2\mu)\mu^2 d\mu = \frac{15}{14} \tag{2.57}$$

The term $R_\infty^0(\mu,\mu_\mathrm{i},\phi)$ can be calculated numerically [16], or approximated in a closed-form formula. In order to approximate $R_\infty^0(\mu,\mu_\mathrm{i},\phi)$, the quantity is represented as a combination of two terms. The first term, $R_\infty^{\mathrm{MS}}$, corresponds to the isotropic scattering that does not depend on the phase function. The second term, $R_\infty^{\mathrm{SS}}$, is proportional to the contribution of single scattering. Therefore,

$$R_\infty^0(\mu,\mu_\mathrm{i},\phi) = R_\infty^{\mathrm{MS}} + R_\infty^{\mathrm{SS}} = C_1\left(\frac{1}{2}+\frac{\mu\mu_\mathrm{i}}{\mu+\mu_\mathrm{i}}\right)+C_2\frac{\Phi(\Theta)}{4(\mu+\mu_\mathrm{i})} \tag{2.58}$$

where $C_1$ and $C_2$ are unknown constants. It is noted that if $C_1 = C_2 = 1$, the expression reduces to the Hapke model. The values of $C_1$ and $C_2$ for liquid water clouds were reported as [54]

$$C_1 = 1 \tag{2.59}$$

$$C_2 = 8 - 4.5\exp\left[-5(\pi-\Theta)\right] - 5\exp\left[-5(\Theta^*-\Theta)\right] \tag{2.60}$$

where $\Theta$ is the scattering angle, and $\Theta^*$ is the rainbow angle which equals 2.4 rad in the visible region. However, the author did not discuss how to determine $C_1$ and $C_2$ for a practical problem. It is noted that $R_\infty^0(\mu,\mu_\mathrm{i},\phi)$ can be converted to the BRDF by using the following expression

$$f_\mathrm{r} = R_\infty^0(\mu,\mu_\mathrm{i},\phi)/\pi \tag{2.61}$$

Similar conversion can be made to $T(\tau_0,\mu,\mu_\mathrm{i})$ to get the BTDF.

## 2.5 Comparison of the Models

All the models discussed above are in closed-forms. These models were used in different areas. Among the directional-hemispherical models, the Kubelka-Munk model and the three-flux model were mainly used in color industry. The adding-doubling model is the most accurate one, and widely used in the study of light scattering in biological tissues. For the study of the bidirectional properties, the Pierce-Marcus model was mainly used for color matching in color industry. The Hapke model and the Sobolev-Kokhanovsky model were developed in the areas of atmosphere science and astrophysics. The applicability of these different models was limited by their assumptions and approximation methods during the development. Table 2.1 compares the ability of these models in terms of three aspects: (1) bidirectional ability; (2) the ability to predict properties of a medium with finite thickness; and (3) the ability to account for anisotropic scattering.

Table 2.1 Comparison of the models of volume scattering

| | Kubelka-Munk | Three-Flux | Adding-Doubling | Hapke | Pierce-Marcus | Sobolev-Kokhanovsky |
|---|---|---|---|---|---|---|
| Bidirectional | No | No | No | Yes | Yes | Yes |
| Finite thickness | Yes | Yes | Yes | No | Yes | Yes |
| Anisotropic | No | No | Yes | Yes | No | Yes |

# CHAPTER 3

# MEASUREMENTS

## 3.1 PTFE Samples

Five sintered Zenith PTFE samples were purchased from Sphere Optics LLC. The thicknesses of Samples 1 to 5 were measured with a micrometer to be $109\ \mu\text{m} \pm 3\ \mu\text{m}$, $259\ \mu\text{m} \pm 3\ \mu\text{m}$, $522\ \mu\text{m} \pm 4\ \mu\text{m}$, $1057\ \mu\text{m} \pm 8\ \mu\text{m}$, and $10.1\ \text{mm} \pm 0.1\ \text{mm}$, respectively. The densities of Samples 1 to 5 were measured to be $1.65\ \text{g/cm}^3 \pm 0.05\ \text{g/cm}^3$, $1.82\ \text{g/cm}^3 \pm 0.05\ \text{g/cm}^3$, $1.90\ \text{g/cm}^3 \pm 0.05\ \text{g/cm}^3$, $1.70\ \text{g/cm}^3 \pm 0.05\ \text{g/cm}^3$, and $1.52\ \text{g/cm}^3 \pm 0.05\ \text{g/cm}^3$, respectively. These samples were cut into $50\ \text{mm} \times 50\ \text{mm}$ pieces from a sheet, except for Sample 5 which came as a $50\ \text{mm} \times 50\ \text{mm}$ piece from the manufacturer.

Surface roughness of the samples was measured using a Digital Instruments Multimode™ Atomic Force Microscope (AFM). The 3D surface scanning images are shown in Fig. 3.1. The area of each sample scanned by the tip of the scanning cantilever was 30 $\mu$m by 30 $\mu$m. The RMSs of the surface roughness of Samples 1 and 2 are 430 nm and 410 nm, respectively. It is noted that there are some deep pitches on the surface that the scanning cantilever tip of the AFM was not able to touch. The influence of these pitches was neglected in the calculation of RMS of the surface roughness.

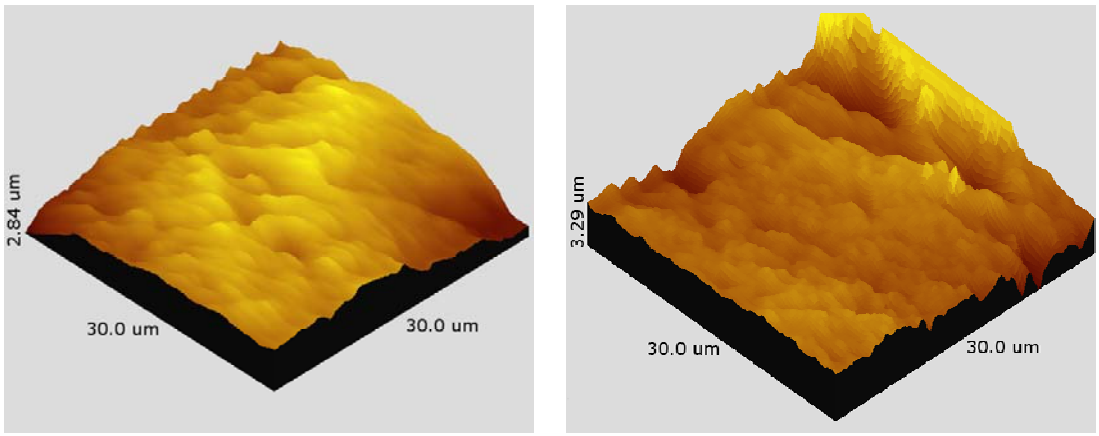


(a) Sample 1 (b) Sample 2

Figure 3.1 Illustration of the surface roughness of Samples 1 and 2 measured using AFM: (a) Sample 1; (b) Sample 2. The scanned area of both samples was 30 $\mu$m by 30 $\mu$m.

### 3.2 Three-Axis Automated Scatterometer

A three-axis automated scatterometer (TAAS) [55] with a 635 nm laser diode was used for the measurement of the BRDF and BTDF. The BRDF is defined as the reflected radiance divided by the incident irradiance, and given as

$$f_{\mathrm{r}} = \frac{dI_{\mathrm{r}}}{I_{\mathrm{i}} \cos\theta_{\mathrm{i}} d\Omega_{\mathrm{i}}} \tag{3.1}$$

where $I_{\mathrm{r}}$ is the reflected radiance, $I_{\mathrm{i}}$ is the incident radiance, $\theta_{\mathrm{i}}$ is the angle of incidence, and $d\Omega_{\mathrm{i}}$ is the solid angle of the incident light. The measurement equation of BRDF is given as [55]

$$f_{\mathrm{r}} = \frac{P_{\mathrm{o}}}{P_{\mathrm{i}} \cos\theta_{\mathrm{o}} \delta\Omega_{\mathrm{o}}} \tag{3.2}$$

where $P_{\mathrm{i}}$ and $P_{\mathrm{o}}$ are the incident and reflected powers reaching the detector respectively, $\theta_{\mathrm{o}}$ is the observation angle (i.e., polar angle of the detector), and $\delta\Omega_{\mathrm{o}}$ is the solid angle

of the detector. The BTDF is defined in a similar way by replacing $I_r$ with $I_t$ (i.e., transmitted radiance) in both equations. A collimation lens was placed in front of the laser diode, resulting in a highly collimated light with a beam divergence less than 0.0126°. A lock-in amplifier (EG&G 7265DSP) was used to produce a modulated voltage signal for the laser diode controller; thus the effects of stray light were minimized. The samples were mounted in a rotary stage so that the incidence angle $\theta_i$ could be changed. A detector controlled by another rotary stage measured the scattered light in an observation angle $\theta_o$ ranging from –90° to 90°. In front of the detector, there was an aperture with a diameter of 8 mm. The distance between the aperture and the sample holder was measured to be $522.5\,\text{mm} \pm 0.5\,\text{mm}$. Consequently, the detector solid angle was $1.84 \times 10^{-4}$ sr and the half cone angle was approximately 0.45° [55]. Since the detector blocked the incident light, the BRDF within $\pm 3°$ of the retroreflection direction could not be measured. The relative uncertainty of the bidirectional property measurements was estimated to be 10% with a confidence level of 95%.

Figure 3.2 shows the schematic of light scattering from a semitransparent film when the light is incident at $\theta_i = 0°$. The observation angle is defined separately for the BRDF and BTDF as depicted in the figure. If the thickness of the sample is less than approximately four times of its radiation penetration depth, the transmitted collimated light (i.e., un-scattered light) can be distinguished from the scattered light in the parallel direction of the incidence. In this case, the measured BTDF should exhibit a noticeable peak at $\theta_o = 0°$.

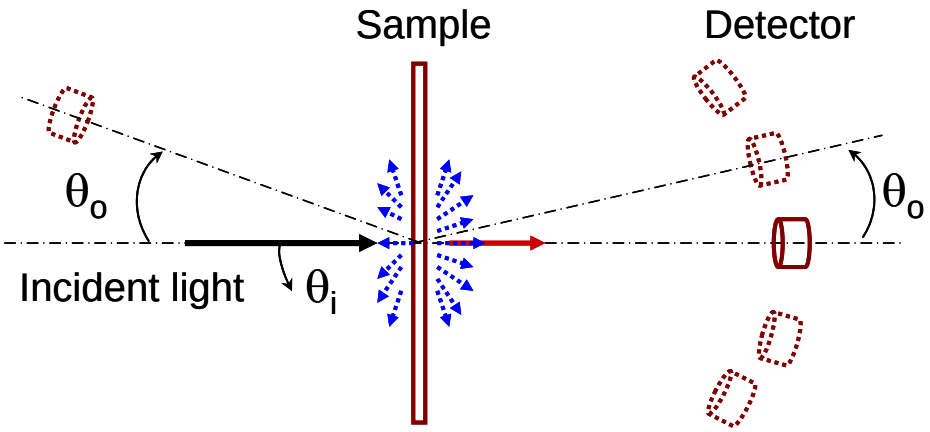


Figure 3.2 A schematic of the volume scattering and the bidirectional property measurement. The dotted lines represent the scattered light and the solid line at the right side of the sample indicates the transmitted collimated (un-scattered) light. The observation angle $\theta_o$ is defined separately for the BRDF and BTDF measurement at a given incidence angle $\theta_i$. The direction in which these angles increase is indicated by arrows.

### 3.3 Integrating Sphere System

The directional hemispherical reflectance and transmittance of the PTFE films were measured by using a monochromator (Oriel Instruments Cornerstone 130) and an integrating sphere (Sphere Optics, Inc). The light source is a tungsten-halogen lamp, whose power output can be adjusted from a power controller. The rotation of two gratings inside the monochromator and the change of filters at the inlet of the monochromator are capable of achieving the resolution of wavelength selection to be as small as 10 nm [56]. The RMS fluctuation of power from the monochromator was estimated to be less than 1%. After the light with the selected wavelength exits the monochromator, it is collimated and directed to the sample through lenses and mirrors. A chopper is used to obtain a phase-locked signal with a high signal-to-noise ratio. The signal is amplified by a trans-impedance pre-amplifier before being sent to a lock-in

amplifier which picks up the phase-locked signal. The integrating sphere has an inner wall of 200 mm in diameter. The entrance port is 25 mm in diameter. The inner wall is coated with PTFE with a reflectance of approximately 0.99 in the visible range [1,56]. A PC based LabView program controls both the acquisition of data from the lock-in amplifier and the selection of wavelengths from the monochromator.

For the measurement of reflectance, the sample to be measured is placed behind the port on the backside of the integrating sphere. For the measurement of transmittance, the sample to be measured is placed in front of the entrance port of the integrating sphere. The detector is placed at another port, and is shielded from the direct incidence of light from samples by a baffle. The relative uncertainty of the measurements of hemispherical reflectance and transmittance was estimated to be 10% with a confidence level of 95%.

# CHAPTER 4

# THEORY AND RESULTS

## 4.1 Modeling the Light Scattering Using RTE

With the assumptions that the medium does not emit light (i.e., cold medium), the wave-like interactions are negligible, the medium is homogeneous, and that the polarization state is neglected, the light scattering in a PTFE film can be modeled using the RTE as

$$\frac{dI(\hat{\mathbf{s}})}{(\sigma+\alpha)ds} = -I(\hat{\mathbf{s}}) + \frac{\omega}{4\pi}\int_{4\pi} I(\hat{\mathbf{s}}_i)\Phi(\hat{\mathbf{s}}_i,\hat{\mathbf{s}})d\Omega_i \tag{4.1}$$

where $I$ is the radiance, $s$ is the physical distance that the light travels, $\omega$ is the scattering albedo defined as $\omega = \sigma/(\sigma+\alpha)$, $\hat{\mathbf{s}}$ and $\hat{\mathbf{s}}_i$ represent the propagation directions of light, $\Omega_i$ is the solid angle, and $\Phi$ is the scattering phase function. In many applications, the Henyey-Greenstein function is used to represent a scattering phase function, and given by [57]

$$\Phi_{HG}(\cos\Theta) = \frac{1-g^2}{(1+g^2-2g\cos\Theta)^{3/2}} \tag{4.2}$$

where the scattering angle $\Theta$ is the angle between the directions of the incident light and the scattered light (i.e., $\cos\Theta = \hat{\mathbf{s}}_i \cdot \hat{\mathbf{s}}$), and $g$ is the asymmetric parameter ranging from $-1$ to 1.

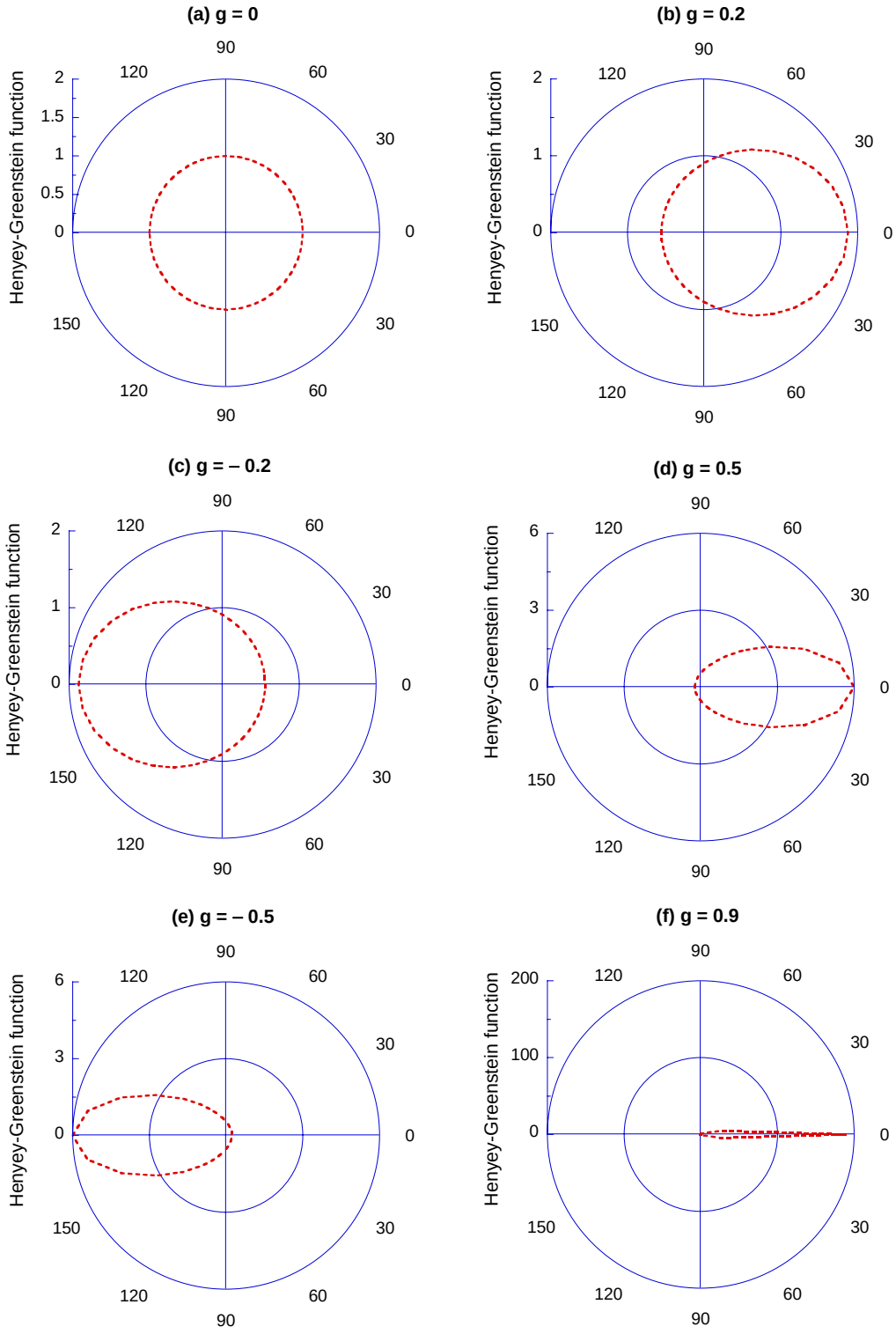


Figure 4.1 Illustration of the shapes of the Henyey-Greenstein function with different values of asymmetric parameter $g$: (a) $g = 0$; (b) $g = 0.2$; (c) $g = –0.2$; (d) $g = 0.5$; (e) $g = –0.5$; (f) $g = 0.9$.

Figure 4.1 shows the shapes of the Henyey-Greenstein function with different values of *g*. The Henyey-Greenstein function yields isotropic scattering for $g = 0$. If $g > 0$, there are more forwardly scattered photon bundles than backward scattered photon bundles. If *g* approaches 1, all photon bundles are scattered in the direction parallel to the incident light. However, if $g < 0$, more photon bundles are scattered backward than forward. If *g* approaches –1, all photon bundles will be scattered in the opposite direction of the incident light.

### 4.2 Adding-Doubling Method and Monte Carlo Simulation

The adding-doubling method and a Monte Carlo simulation were employed to solve the RTE for PTFE films. Originally introduced by van de Hulst [41], the adding-doubling method is used to solve the RTE in a parallel slab for the prediction of its directional-hemispherical properties. More detailed discussion of the adding-doubling method is given in Section 2.2.3. Since the adding-doubling method cannot predict the BRDF and BTDF, a Monte Carlo simulation was developed to model the volume scattering.

In the Monte Carlo simulation, the propagation of each photon bundle is represented by the position vector (**r**) and the propagation direction vector ($\hat{\mathbf{s}}$) in a global coordinate as shown in Fig. 4.2(a). The medium with thickness *d* is located between plane $z = 0$ and $z = d$. In order to simulate a collimated light incidence, each photon bundle hits the origin with a fixed incidence angle $\theta_i$. The plane of incidence is set to be *x*-*z* plane without loss of the generosity, i.e., $\hat{\mathbf{s}}_i = \cos\theta_i \hat{\mathbf{x}} + \sin\theta_i \hat{\mathbf{y}}$. Notice that the surface

scattering effects due to the interface between media with different refractive index values have not been considered in the present study. Therefore, each photon bundle penetrates the medium in a certain distance and then starts to be scattered. Each scattering event is completely volume scattering which is independent on the number of particles. In other words, the mean-free-path of the photons should be greater than the wavelength of the photons.

After the photon bundle is released, the step size of the initial propagation or between subsequent scattering events is calculated by

$$l = -\frac{1}{\sigma + \alpha} \ln(R_1) \tag{4.3}$$

where $\sigma$ is the scattering coefficient, $\alpha$ is the absorption coefficient, and $R_1$ is a uniform random number between 0 and 1, which is generated based on the quasi-random sequence [58,59]. This equation guarantees the mean-free-path of a photon bundle to be $1/(\sigma + \alpha)$.

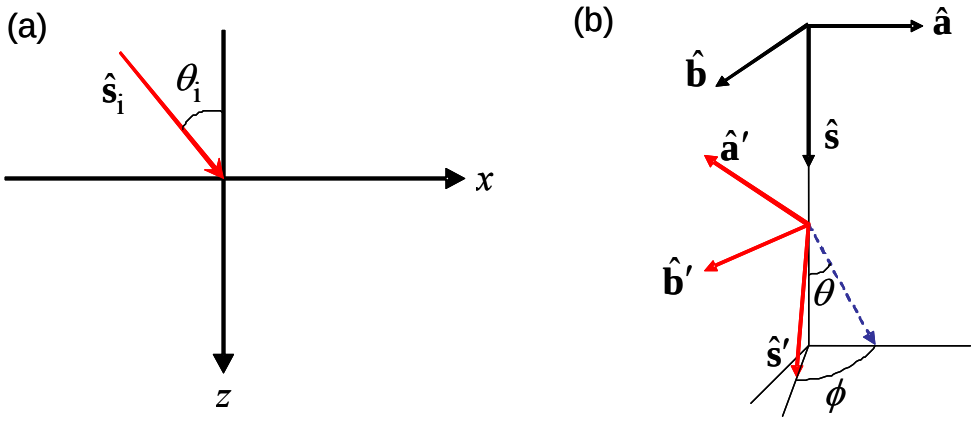


Figure 4.2 The relationship of the direction vectors of a photon bundle after a scattering event ($\hat{\mathbf{s}}'$) and before a scattering event ($\hat{\mathbf{s}}$): (a) the global coordinate and the direction vector of the incident light; (b) direction vectors of a photon bundle before and after a scattering event. The direction vectors are described by polar angle $\theta$ and the azimuth angle $\phi$ relative to the local coordinate ($\hat{\mathbf{a}}$, $\hat{\mathbf{b}}$, $\hat{\mathbf{s}}$) that is fixed on the photon bundle.

The direction of the photon bundle ($\hat{\mathbf{s}}'$) after a scattering event is described by the polar angle $\theta$ and the azimuth angle $\phi$ with respect to the direction vector $\hat{\mathbf{s}}$ before the scattering event, as shown in Fig. 4.2(b). The azimuth angle is assumed to be uniform (i.e., the scattering is isotropic in the azimuthal direction). The polar angle can be determined from a scattering phase function. In the present study, the Henyey-Greenstein scattering function [57] is employed. Therefore, $\cos\theta$ can be obtained with a generated uniform random number $R_2$ as [60]

$$\cos\theta = \begin{cases} \dfrac{1}{2g}\left[1+g^2-\left(\dfrac{1-g^2}{1-g+2gR_2}\right)^2\right] & \text{if } g \neq 0 \\ 2R_2 - 1 & \text{if } g = 0 \end{cases} \tag{4.4}$$

where $g$ is the asymmetric parameter. The azimuth angle is determined by $\phi = 2\pi R_3$ with another random number $R_3$. Once $\theta$ and $\phi$ are determined, the direction vector after scattering $\hat{\mathbf{s}}'$ is determined in the local coordinate ($\hat{\mathbf{s}}$, $\hat{\mathbf{a}}$, and $\hat{\mathbf{b}}$). The vector $\hat{\mathbf{b}}$ directs the reference zero for the azimuth angle $\phi$. First, the $\hat{\mathbf{s}}$ is rotated counterclockwise with respect to the vector $\hat{\mathbf{b}}$ by $\theta$. The resulting vector is then rotated counterclockwise with respected to the vector $\hat{\mathbf{s}}$ by $\phi$.

$$\hat{\mathbf{s}}' = \cos\theta\,\hat{\mathbf{s}} + \sin\theta\cos\phi\,\hat{\mathbf{a}} + \sin\theta\sin\phi\,\hat{\mathbf{b}} \tag{4.5}$$

$$\hat{\mathbf{a}}' = -\sin\theta\,\hat{\mathbf{s}} + \cos\theta\cos\phi\,\hat{\mathbf{a}} + \cos\theta\sin\phi\,\hat{\mathbf{b}} \tag{4.6}$$

The new position vector of the photon bundle is thus, $\mathbf{r}' = \mathbf{r} + l\hat{\mathbf{s}}'$. The energy of the photon bundle reduces to $E' = \omega E$, where $E$ is the energy of the photon bundle before the scattering event. The photon bundle is considered to be reflected from or transmitted

through the medium if the projection of the position vector on the $z$ axis is less than zero or greater than $d$, respectively.

In the Monte Carlo simulation, the directional-hemispherical reflectance is calculated as the summation of the energy of the reflected photon bundles divided by the total number of photon bundles. Similarly, the directional-hemispherical transmittance is calculated as the summation of the energy of the transmitted photon bundles divided by the total number of photon bundles. The calculated $R$ using the Monte Carlo simulation with a photon bundle number of $1\times10^6$ is in agreement with that using the adding-doubling method within a statistical fluctuation of 0.5%. In order to determine the BRDF and BTDF, an imaginary detector with a solid angle of $1.76\times10^{-3}$ sr is placed in 5° intervals in the corresponding hemisphere. Similar to the actual measurement, the total energy received by the imaginary detector at each position is determined by the number of photon bundles that hit the detector during the simulation. For the calculation of BRDF and BTDF, $2\times10^7$ photon bundles are used and each run takes approximately 2.5 hours of CPU time with a 3.2 GHz Pentium 4 processor when the thickness of the sample is 0.1 mm. The resulting relative uncertainty between the BRDF/BTDF and their fitting curves is around 1.5 %.

## 4.3 Determination of Coefficients Used in RTE

### 4.3.1 Determination of the reduced scattering coefficient

From the adding-doubling method and Monte Carlo simulation, it is found that the scattering coefficient, $\sigma$, and the asymmetric parameter $g$ are coupled. If the

absorption coefficient is negligible, then the reflectance and transmittance of a sample only depend on the physical thickness of the sample and the reduced scattering coefficient $\sigma' = \sigma(1-g)$.

Figure 4.3 shows the relationship between the directional hemispherical reflectance and the asymmetric parameter $g$ of the scattering phase function when the reduced scattering coefficient is fixed at $167\,\mathrm{cm}^{-1}$. Both the Monte Carlo simulation and the adding-doubling method produce a directional hemispherical reflectance of 0.48 regardless of the $g$ value. The Monte Carlo simulation was performed 5 times at each $g$ value. The standard deviation of the Monte Carlo simulation result at each $g$ value is less than 0.0006.

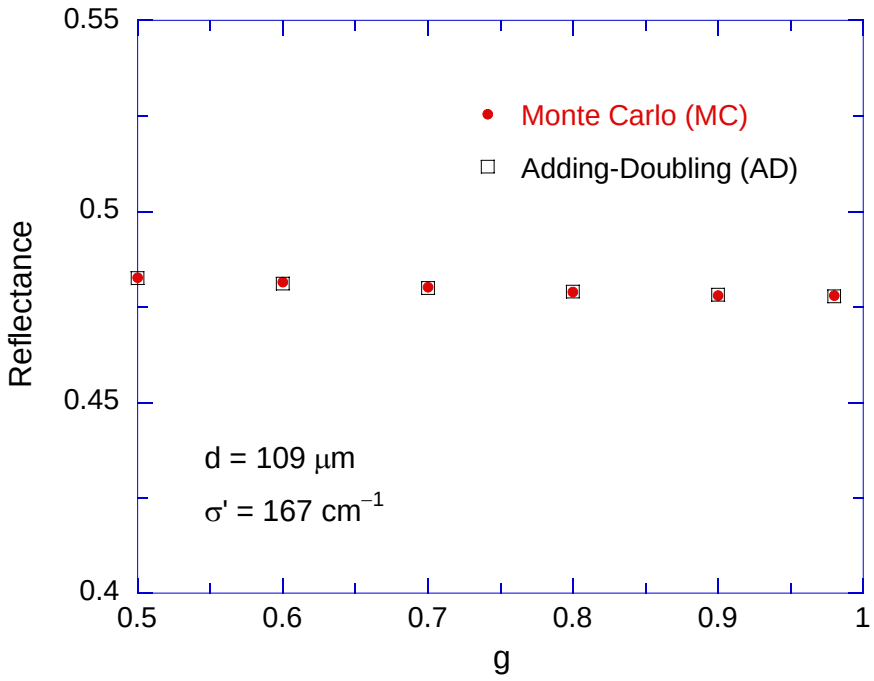


Figure 4.3 The coupling of $\sigma$ and $g$. The sample thickness is 109 $\mu$m. The reduced scattering coefficient is $167\,\mathrm{cm}^{-1}$. The squares represent calculation using the adding-doubling method. The dots represent the Monte Carlo simulation.

If the absorption coefficient is negligible, the directional-hemispherical properties of the PTFE films depend only on the film thickness and the reduced scattering coefficient [42]. In order to estimate $\sigma$, the directional-hemispherical properties were obtained by integrating the measured BRDF and BTDF over the hemisphere. Figure 4.4 shows the measured and fitted BTDF of Sample 1 at normal incidence. For Sample 1, eight measurements were conducted at different locations on the sample for each observation angle. Figure 4.4(a) shows the eight measurements of the BTDF in the range of observation angle from 0° to5°. The dashed lines show the error bounds with 95% confidence interval. Figure 4.4(b) shows the average of the measured BTDF (circles) and the fitted (solid line) BTDF of Sample 1 at normal incidence. The measurement was conducted by moving the detector from $\theta_o = 0$ to 5° in 1° increments and from 5° to 78° in 3° increments. Error bars standing for the measurement uncertainty of 95% confidence interval were also plotted. The measured results beyond 78° are not reliable because of the alignment error.

Since the measured BTDF exhibits some fluctuations due to the measurement uncertainty and sample inhomogeneity, a quadratic equation is used to fit the BTDF data. The standard error of estimate (SEE) of the fitted equation is $1.5\times10^{-3}$ sr$^{-1}$. Notice that the extrapolation of the fitted equation in the $\theta_o$ range from 78° to 90° is performed before the integration and the relative error of the extrapolation is estimated to less than 0.5%. In addition, the BTDF is assumed to be symmetric with respect to $\theta_o = 0$. The directional-hemispherical properties of Sample 1 and other samples were obtained by integrating the fitted equations over the corresponding hemisphere.

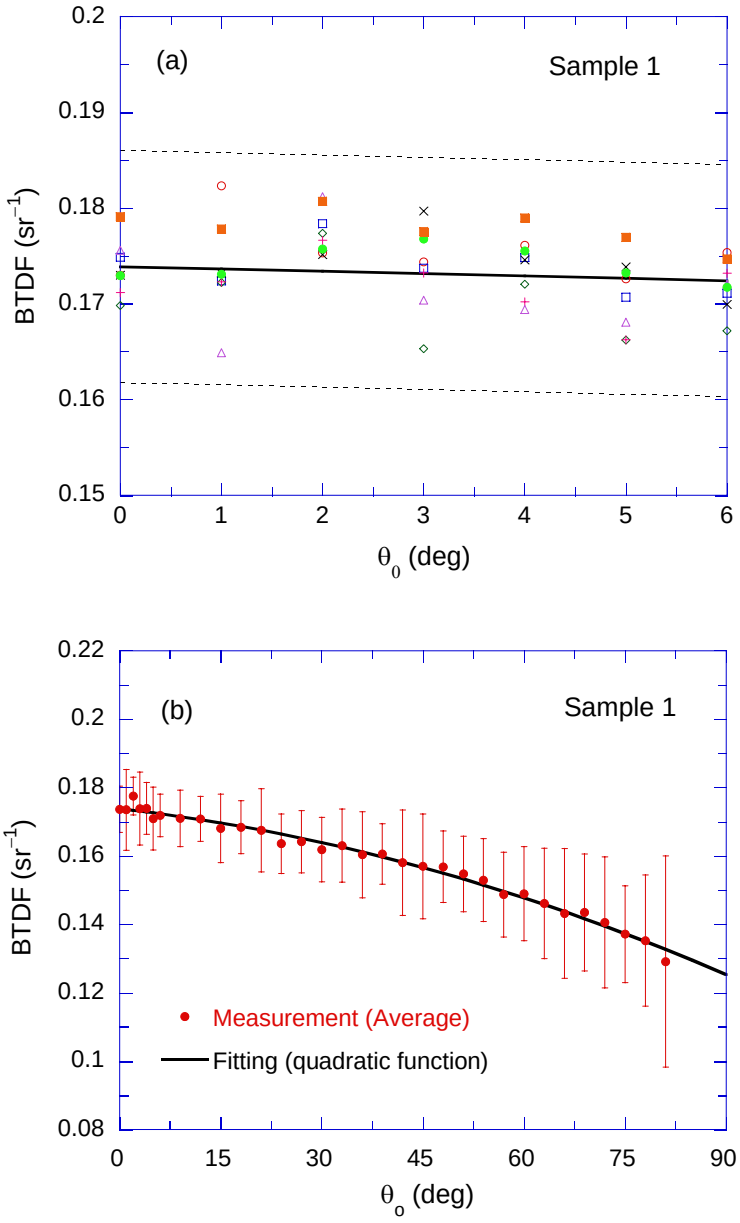


Figure 4.4 BTDF of Sample 1 at normal incidence: (a) eight measurements at each observation angle in the range from 0° to 6°; (b) average of the eight measurements in the range of observation angle from 0° to 90°. The markers represent the measured data and the solid line indicates the fitted quadratic equation. The dashed lines show the error bounds with 95% confidence interval. The error bars show the uncertainty of eight measurements at each observation angle with 95% confidence interval.

**Table 4.1** The directional-hemispherical reflectance and transmittance of the PTFE samples obtained by integrating the measured BRDF and BTDF at normal incidence.

| | Sample 1 | Sample 2 | Sample 3 | Sample 4 |
|---|---|---|---|---|
| *R* | 0.591 | 0.766 | 0.871 | 0.976 |
| *T* | 0.451 | 0.299 | 0.190 | 0.095 |
| *R*+*T* | 1.042 | 1.065 | 1.061 | 1.071 |
| *R*/*T* | 1.310 | 2.562 | 4.584 | 10.383 |

Table 4.1 lists the calculated reflectance and transmittance of Samples 1 to 4 based on the measured BRDF and BTDF. It is noted that the summation of *R* and *T* for Samples 1 to 4 is consistently greater than unity by approximately 7%. This is due to the biased uncertainty of the scatterometer. The reduced scattering coefficient can be obtained by fitting *R*/*T* of Samples 1 to 4 using the adding-doubling method with the measured thicknesses. The ratio of *R*/*T,* instead of *R* and *T*, is chosen because the biased uncertainty can be cancelled out in the ratio if the effect of the biased uncertainty is the same in the BRDF and BTDF measurements.

Figure 4.5 shows the *R*/*T* ratio based on the measured BRDF and BTDF and calculated values using the adding-doubling method with the best fitted $\sigma'$. The circles represent the measured data and the triangles indicate the calculated values. The SEE between the measured and the calculated *R*/*T* values reaches the minimum of 0.355 around $\sigma' = 167\ \text{cm}^{-1}$. Considering the measurement uncertainty, the reduced scattering coefficient is estimated to be $\sigma' = 167\ \text{cm}^{-1} \pm 20\ \text{cm}^{-1}$. In this $\sigma'$ range, the *R*/*T* value will vary by approximately ±13%. Here, the obtained $\sigma'$ value is approximately one order of magnitude higher compared to the reported value in Ref. [29].

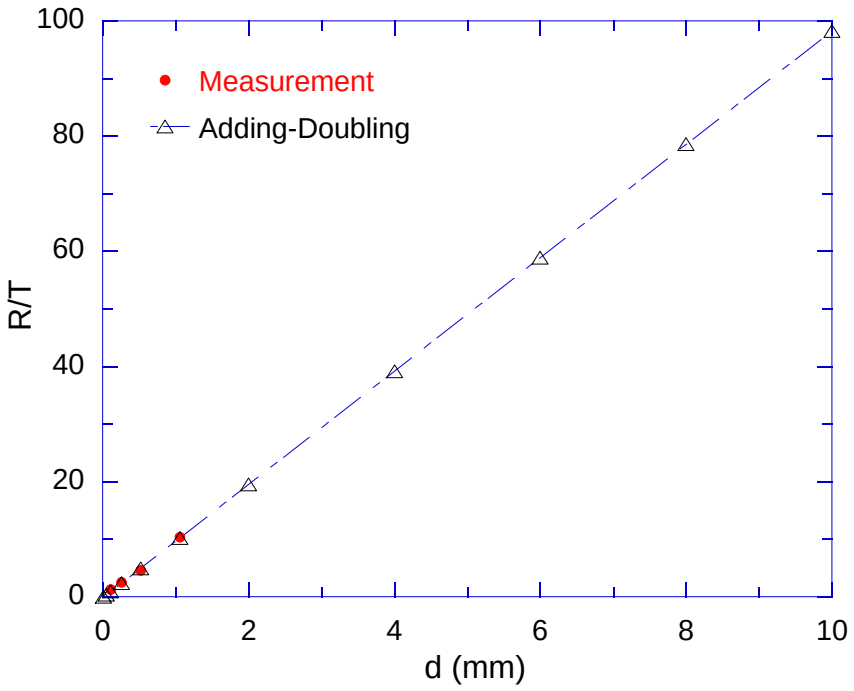


Figure 4.5 The ratio of *R/T* obtained from the integration of measured BRDF and BTDF (circles) and that calculated using adding-doubling method (squares). The parameters used for calculation are $\sigma' = 167$ cm$^{-1}$ and $g = 0.9$.

While in general the reflectance and transmittance are complicated functions of the film thickness, the ratio *R*/*T* exhibits a linear dependence on the film thickness. In Fig. 4.5, the calculated *R*/*T* values are intentionally extended to the thickness of 10 mm. It can be clearly seen that the *R*/*T* ratio is in linear relationship with the film thickness from 0.1 mm to 10 mm. The measurements also follow the linear trend although there are some deviations from the predicted value. A linear regression shows that the linear relationship between *R*/*T* and the film thickness can be represented by $R/T = 0.59\sigma' d$. From the calculations using different values of the reduced scattering coefficient, it shows that the constant of 0.59 does not depend on the reduced scattering coefficient. The linear regression line is denoted by the dashed-dot line in the figure.

It is noted that for highly scattering and non-absorbing medium, the linear dependency of $R/T$ on $\sigma' d$ can be derived from some approximation models such as the Kubelka-Munk model (i.e., two flux model) [31,32] and the three flux model [13]. Star et al. [61] reported the transformation between the scattering coefficient used in the Kubelka-Munk model and the scattering coefficient $\sigma$ of RTE. By solving the governing equations of these models, it shows that the ratio of $R/T$ is in linear relationship with $\sigma' d$ similar as that calculated using the adding-doubling method. The linear dependency of $R/T$ on film thickness for highly scattering and non-absorbing medium can be obtained from all these models including the adding-doubling method, Monte Carlo simulation, Kubelka-Munk model, and the three flux model. Although there are some variations in the final analytical expressions depending on different models and approximations, the linear relationship provides a very simple approach for the determination of the reduced scattering coefficient of PTFE films by measuring $R$ and $T$ of a sample with known thickness. The linearity of $R/T$ will be discussed in detail in Section 4.3.4.

### 4.3.2 Estimation of the absorption coefficient

Table 4.2 lists the calculated $R$ and $T$ of the 10-mm-thick PTFE slab using the adding-doubling method. The parameters are set to be $\sigma' = 167\ \text{cm}^{-1}$ and $g = 0.9$ (i.e., $\sigma = 1670\ \text{cm}^{-1}$). As mentioned in the previous section, the reduced scattering coefficient is the dominant factor in determining the hemispherical properties. Hence, the calculation shown in Table 4.2 is also applicable for different $g$ values as long as $\sigma'$ is fixed. The absorption coefficient is determined to be less than $0.01\ \text{cm}^{-1}$ by assuming the

directional-hemispherical reflectance of the 10-mm-thick sample to be greater than 0.977. It should be noted that the measured values are usually greater than 0.98 [6]. Since the obtained absorption coefficient is at least four orders of magnitude smaller than the scattering coefficient, the absorption in PTFE films is neglected hereafter.

In Table 4.2, the adding-doubling calculation suggests that the 10-mm-thick slab can have a non-zero transmittance as large as 0.001 when the absorption is neglected. In order to assess the transmittance value, the directional-hemispherical transmittance of Sample 5 was measured using the integrating sphere with a 635 nm laser diode as the light source. From the integrating sphere measurements, the transmittance of 10-mm-thick slab is estimated to be $0.007 \pm 0.002$, which indicates that the absorption coefficient should be less than $0.01\ \text{cm}^{-1}$ (refer to Table 4.2). The uncertainty associated with the integrating sphere was greater than the scatterometer. Therefore, it was not used to measure the directional-hemispherical properties of the samples in the previous section.

**Table 4.2** The influence of the absorption coefficient on the directional-hemispherical reflectance and transmittance of the 10-mm-thick PTFE slab when $\sigma = 1670\ \text{cm}^{-1}$ and $g = 0.9$.

| $\alpha\ (\text{cm}^{-1})$ | $\omega$ | $R$ | $T$ |
|---|---|---|---|
| 0.0000 | 1.00000000 | 0.9899 | 0.0101 |
| 0.0001 | 0.99999994 | 0.9898 | 0.0100 |
| 0.0010 | 0.99999940 | 0.9883 | 0.0093 |
| 0.0050 | 0.99999701 | 0.9827 | 0.0068 |
| 0.0070 | 0.99999581 | 0.9803 | 0.0059 |
| 0.0100 | 0.99999401 | 0.9770 | 0.0048 |
| 0.1000 | 0.99994012 | 0.9307 | 0.0001 |

### 4.3.3 Ranges of the scattering coefficient and the asymmetric parameter

If the collimated light transmittance $T_c$ is available, the scattering coefficient can be easily determined by using Beer's law, $T_c = \exp(-\sigma d)$. In most cases, however, the collimated light transmittance cannot be measured unless the thickness of the PTFE sample is less than 30 $\mu$m which is approximately four times the mean free path. Although the collimated light transmittance was not observed for the PTFE samples due to their relatively large thicknesses, a range of the scattering coefficient of PTFE as well as the approach that was used to determine this range are reported in this section.

As discussed earlier, Fig. 4.4 shows the measured and fitted BTDF of Sample 1 at normal incidence. At each observation angle, the BTDF was measured eight times at different locations of Sample 1 by rotating the sample 45° after each measurement. Since the laser beam was not pointing at the center of the sample, the location of the laser spot changed when the sample was rotated. For the other samples, only one measurement was conducted at a fixed location. Figure 4.4(a) shows the eight measured BTDF values with different markers at each observation angle in the range from 0° to 6°. The fitted curve and the error bounds with 95% confidence interval were also shown in the figure. Figure 4.4(b) shows the average of the eight measured BTDF values at each observation angle and the fitted curve in the range from 0° to 90°. The error bars show the measurement uncertainty with 95% confidence interval. The average uncertainty of BTDF is estimated to be $0.012\ \text{sr}^{-1}$, and could be from the instrument as well as the inhomogeneity of the sample.

As can be seen in Fig. 4.4, the BTDF of the 109-$\mu$m-thick sample does not show a peak at $\theta_o = 0°$, suggesting that the transmitted collimated light is overwhelmed by the

scattered light in the parallel direction to the incidence. Because the difference of BTDF between the 0° observation angle and its adjacent angles is negligible comparing with the measurement uncertainty, the BTDF due to collimated light transmittance must be less than the uncertainty. Otherwise, a distinguishable peak should appear at 0° in Fig. 4.4. Therefore, the upper limit of the collimated light transmittance can be obtained by multiplying the solid angle of the detector and the uncertainty of the BTDF measurement. Using the Beer's law, the lower limit of the scattering coefficient is estimated to be $1200\ \mathrm{cm}^{-1}$.

Under the condition that the wave-like interactions and the dependent scattering are negligible, the mean free path should be greater than the wavelength of incident light. It is assumed that the mean free path is 2 $\mu$m, which is approximately three times the wavelength of the laser (i.e., 635 nm). With this assumption, the upper limit of the scattering coefficient is determined to be $5000\ \mathrm{cm}^{-1}$. Based on the reduced scattering coefficient and the range of the scattering coefficient, the asymmetric parameter should be between 0.861 and 0.967, suggesting that PTFE is a highly forward scattering material. Comparing with the parameters of biological tissues, the scattering coefficient of PTFE is approximately ten times larger [28].

### 4.3.4 The linearity of R/T

It is noted that for highly scattering, non-absorbing medium, the linear dependency of $R/T$ on film thickness can be derived from light scattering models such as the Kubelka-Munk model (i.e., two flux model) [31,32] and the three flux model [13]. If

the absorption is negligible, the reflectance and transmittance calculated using the Kubelka-Munk model can be reduced to

$$R = \frac{S_{\mathrm{KM}} d}{S_{\mathrm{KM}} d + 1} \tag{4.7}$$

$$T = \frac{1}{S_{\mathrm{KM}} d + 1} \tag{4.8}$$

where $S_{\mathrm{KM}}$ is the scattering coefficient in the Kubelka-Munk model, and $d$ is the thickness of the medium. Star et al. [61] found that the transformation between the Kubelka-Munk scattering coefficient $S_{\mathrm{KM}}$ and the scattering coefficient $\sigma$ of RTE is $S_{\mathrm{KM}} = \left[3\sigma(1-g) - \alpha\right]/4$. Therefore, the Kubelka-Munk model produces $R/T = 0.75\sigma' d$. Note that from adding-doubling calculation, the constant is 0.59 instead of 0.75. This difference could be due to the simplification of the Kubelka-Munk model.

Comparing with the Kubelka-Munk model that assumes the incidence of diffuse light on the medium, the three flux model considers the incidence of collimated light. By assuming isotropic scattering phase function (i.e., $g = 0$ or $\sigma = \sigma'$) and non-absorption conditions, the three flux model can be expressed in the following equations

$$\frac{dF_1}{dx} = -\sigma F_1 \tag{4.9}$$

$$\frac{dF_2}{dx} = \frac{\sigma}{2} F_1 - SF_2 + SF_3 \tag{4.10}$$

$$\frac{dF_3}{dx} = -\frac{\sigma}{2} F_1 + SF_2 - SF_3 \tag{4.11}$$

where $F_1$, $F_2$, and $F_3$ are the collimated flux, diffuse flux in the forward direction, and diffuse flux in the backward direction, respectively, $\sigma$ is the scattering coefficient used

in RTE, $S$ is the scattering coefficient from a diffuse flux in one direction to the diffuse flux of the opposite direction, and $x$ represents the coordinate. With boundary condition $F_1(0) = 1$ (i.e., the incident light flux equals 1), it is found that $F_1 = e^{-\sigma x}$. $F_2$ and $F_3$ can be solved using boundary conditions $F_2(0) = 0$ and $F_3(d) = 0$. Here, $d$ is the thickness of the medium. The reflectance, diffuse light transmittance, and collimated light transmittance are expressed as: $R = F_3(0)$, $T_\mathrm{d} = F_2(d)$, and $T_\mathrm{c} = F_1(d)$, respectively. The transmittance ($T$) is the summation of the diffuse light transmittance ($T_\mathrm{d}$) and the collimated transmittance ($T_\mathrm{c}$). In the case of $\sigma d >> 1$, the exponential term $e^{-\sigma d}$ appears during the derivation can be neglected, and the ratio of $R/T$ calculated using the three flux model can be reduced to

$$\frac{R}{T} = \frac{2S}{2S+\sigma}\sigma d - \frac{2S-\sigma}{2S+\sigma} \tag{4.12}$$

For isotropic scattering phase function [13], $S = 0.75\sigma$, Eq. (4.12) reduces to

$$R/T = 0.6\sigma d - 0.2 \tag{4.13}$$

In the case of $\sigma d << 1$, the exponential term appears during the derivation can be approximated as $e^{-\sigma d} = 1 - \sigma d$. Then the ratio of $R/T$ calculated using the three flux model can be approximated as

$$\frac{R}{T} = \frac{\sigma}{2S-3\sigma}\sigma d = 0.67\sigma d \tag{4.14}$$

The linear dependency of $R/T$ on film thickness for highly scattering, non-absorbing medium can be derived from all these light scattering models including the adding-doubling method, Monte Carlo simulation, Kubelka-Munk model, and the three flux model. There are some variations in the final analytical forms of the expressions

depending on different models and approximations used during the derivation. Actually, from the calculation using the adding-doubling method, the linearity between *R/T* and $\sigma' d$ changes with the range of $\sigma' d$: (1) In the range of $\sigma' << 1$ (i.e., $0.02 << \sigma' d << 0.17$), the equation is $R/T = 0.26\sigma' d$; (2) In the range of $\sigma' d$ around 1 (i.e., $0.3 << \sigma' d << 9$), the equation is $R/T = 0.58\sigma d - 0.13$; and (3) In the range of $\sigma' d >> 1$ (i.e., $18 << \sigma' d << 1670$), the equation is $R/T = 0.59\sigma' d$.

This linear relationship between the *R/T* ratio and $\sigma' d$ provides a very simple approach for the determination of the reduced scattering coefficient of PTFE films. Theoretically, the measurement of *R* and *T* of just one sample with known thickness is enough for the determination of the reduced scattering coefficient. Because of its superiority in both accuracy and efficiency, the adding-doubling method is used here for the calculation of the *R/T* ratio.

### 4.4 Comparison of BRDF and BTDF between Models and Measurements

Figure 4.6 shows the measured and calculated BRDF of Samples 1 to 5 at normal incidence. The observation angle ranges from −75° to 75°. Different from the measurement of BTDF in Fig. 4.4, the BRDF of Samples 1 to 5 was measured in 10° intervals except for $\theta_o = \pm 5°$. The solid lines represent the fitted polynomial curves of BRDF with a SEE less than $0.008\,\mathrm{sr}^{-1}$ and $0.004\,\mathrm{sr}^{-1}$ for the measured values and calculated values, respectively.

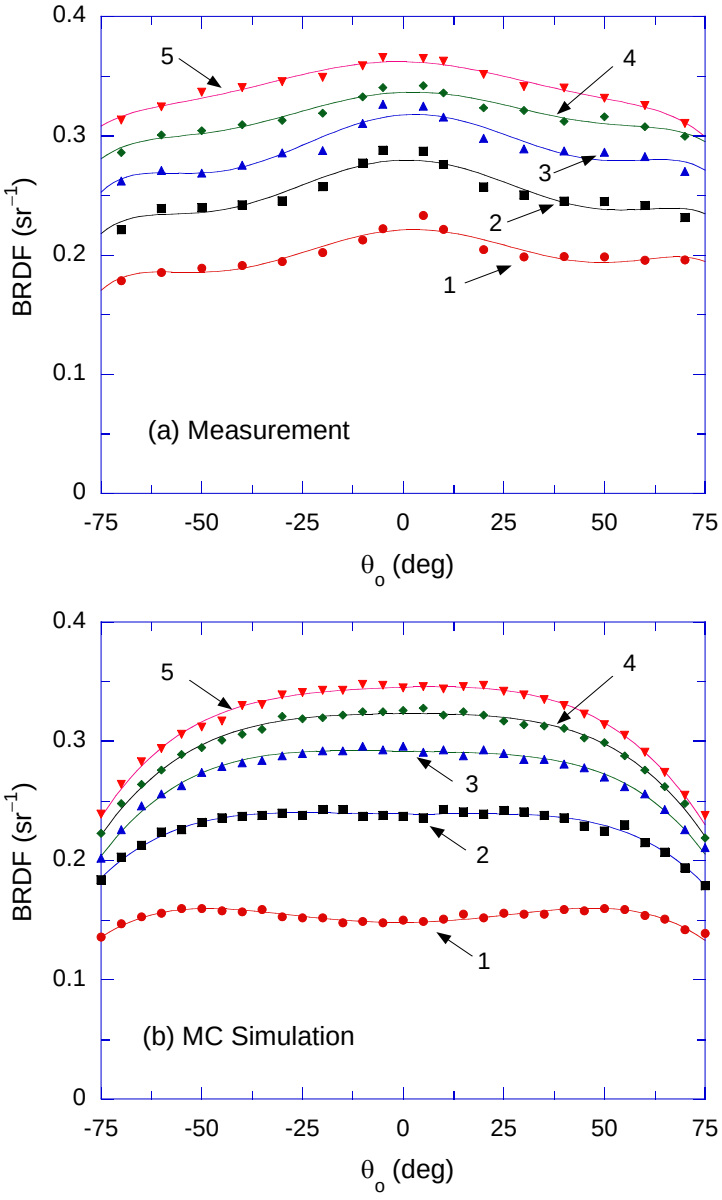


Figure 4.6 BRDF of all samples at normal incidence: (a) measurement; (b) Monte Carlo simulation. The symbols represent the measured and calculated values. The solid lines represent fitted curves of BRDF. The numbers with arrows indicate the corresponding sample.

The measured BTDF in Fig. 4.6(a) exhibits nearly diffuse characteristics. For instance, the BRDF of the 10-mm-thick sample varies from $0.30\ \mathrm{sr}^{-1}$ to $0.37\ \mathrm{sr}^{-1}$ in the considered $\theta_o$ range. For an opaque, nonabsorbing, and perfectly diffuse reflector, the BRDF should be a constant of $0.318\ \mathrm{sr}^{-1}$. The slightly larger variation of the BRDF of Sample 5 compared to the perfect diffuser is mainly due to the hump near $\theta_o = 0°$. In a round robin test of the PTFE material, Early et al. [62] also reported similar variation of the BRDF of opaque PTFE samples at normal incidence. As the sample thickness decreases, the corresponding BRDF value decreases because of the increased transmission. Interestingly, the hump in the BRDF near $\theta_o = 0°$ becomes more obvious as the thickness decreases. Due to the measurement uncertainty of the laser scatterometer, the measured BRDF does not exhibit perfect symmetry with respect to $\theta_o = 0°$.

The predicted BRDF using the Monte Carlo simulation is plotted in Fig. 4.6(b). In the calculation hereafter, the parameters of RTE are set to be $\sigma' = 167\,\mathrm{cm}^{-1}$ and $g = 0.9$. Compared with the measurements, the Monte Carlo simulation is able to predict the general trend of the BRDF. The Monte Carlo results do not show the hump near $\theta_o = 0°$ for all samples. This suggests that the hump in the measured BRDF may be caused by surface scattering effects due to the refractive index mismatch, which is not considered in the simulation. Although the directional-hemispherical properties predicted by the Monte Carlo simulation agree very well with the measurements, the bidirectional properties show some deviations due to the simplicity of the model.

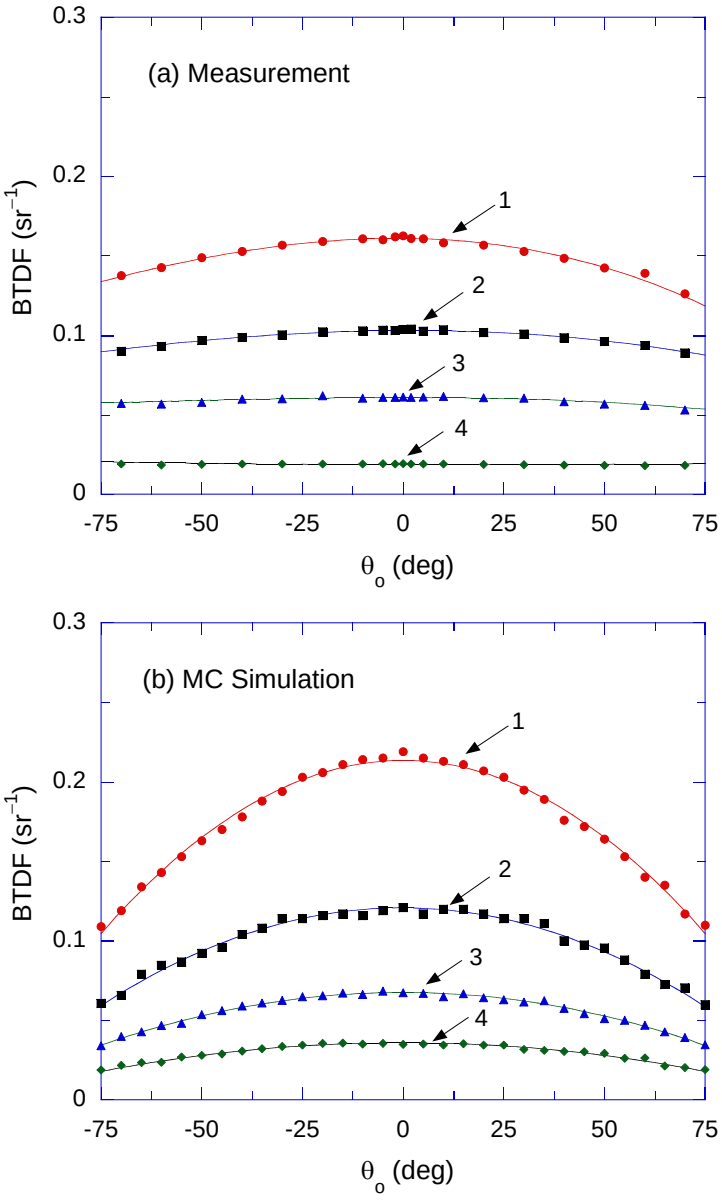


Figure 4.7 BTDF of Samples 1 to 4 at normal incidence: (a) measurement; (b) Monte Carlo simulation. The symbols represent the measured and calculated values. The solid lines represent fitted curves of BTDF. The numbers with arrows indicate the corresponding sample.

Figure 4.7(a) shows the measured BTDF of Samples 1 to 4 at normal incidence. Since the transmittance of Sample 5 is less than 0.01, the BTDF of Sample 5 is not reported here. The solid lines represent fitted polynomial curves of BTDF with a SEE less than $0.003\,\mathrm{sr}^{-1}$ for both the measured values and calculated values. As expected for Samples 1 to 4, the BTDF increases when the sample thickness decreases. The measurements reveal that the BTDF of each sample appears flatter than the BRDF. This can be explained by the multiple scattering of photon bundles inside the film. In order for the photon bundles to transmit through the PTFE films, they need to experience numerous scattering events, resulting in random propagation in the medium. Therefore, the BTDF of Sample 4 with thickness of 1 mm is nearly uniform in the considered observation angle range.

Figure 4.7(b) shows the Monte Carlo simulation of BTDF. The calculated BTDF captures the essential features of the measured BTDF. On the other hand, there exist larger deviations between the calculated and measured BTDF for thinner samples. For Sample 1, the calculated BTDF varies from $0.11\,\mathrm{sr}^{-1}$ to $0.21\,\mathrm{sr}^{-1}$, but the measured BTDF is relatively flat.

The effects of incidence angle on the BRDF are shown in Fig. 4.8. Figure 4.8(a) shows the measured BRDF of Sample 2 at incidence angles of 0°, 30°, 50°, and 70°. The measurements were performed with a linear polarizer to separate the polarization state of the light at oblique incidence. In the present paper, the polarization-dependent volume scattering is not considered, and the measured BRDF is the average of p- and s-polarizations. At oblique incidence, the measured BRDF exhibits specular peaks, which become more obvious if $\theta_o > 50°$. Such specular peaks in the BRDF are generally

observed in the surface scattering from rough samples [63]. The measurements at oblique incidence angles suggest that the surface scattering effect may exist in the studied PTFE samples. The BRDF for backscattering (i.e., $\theta_o < 0°$) decreases as the incidence angle increases.

As shown in Fig. 4.8(b), the Monte Carlo simulation is in reasonable agreement with the measurements. It is noted that the calculated BRDF follows the reciprocity principle. However, since the surface scattering effect is not included in the simulation, the predicted BRDF does not have specular peaks. It can be seen that the predicted BRDF at $\theta_i = 50°$ and 70° continuously increases as $\theta_o$ increases. This feature in the BRDF can be explained by the highly forward scattering phase function. As photon bundles hit the top surface of the PTFE film at larger incidence angles, more photon bundles will penetrate only a very shallow depth and scatter much less before leaving the top surface than those at normal incidence. Hence, the BRDF at oblique incidence increases as the observation angle becomes larger.

The deviation of the calculation from the measurement is attributed to the complexity of actual volume scattering in the PTFE films. It is important to note that the Henyey-Greenstein phase function is only an approximation and may not fully capture the real scattering phase function of PTFE. Although the Henyey-Greenstein phase function has also been used to model the scattering of snow, the rigorous modeling and measurement demonstrated that the phase function of snow has some irregularities which cannot be depicted by the Henyey-Greenstein function [64]. Furthermore, the Monte Carlo simulation does not consider wave-like interactions in the scattering. Nevertheless, the simple volume scattering model captures the general trend of the BRDF.

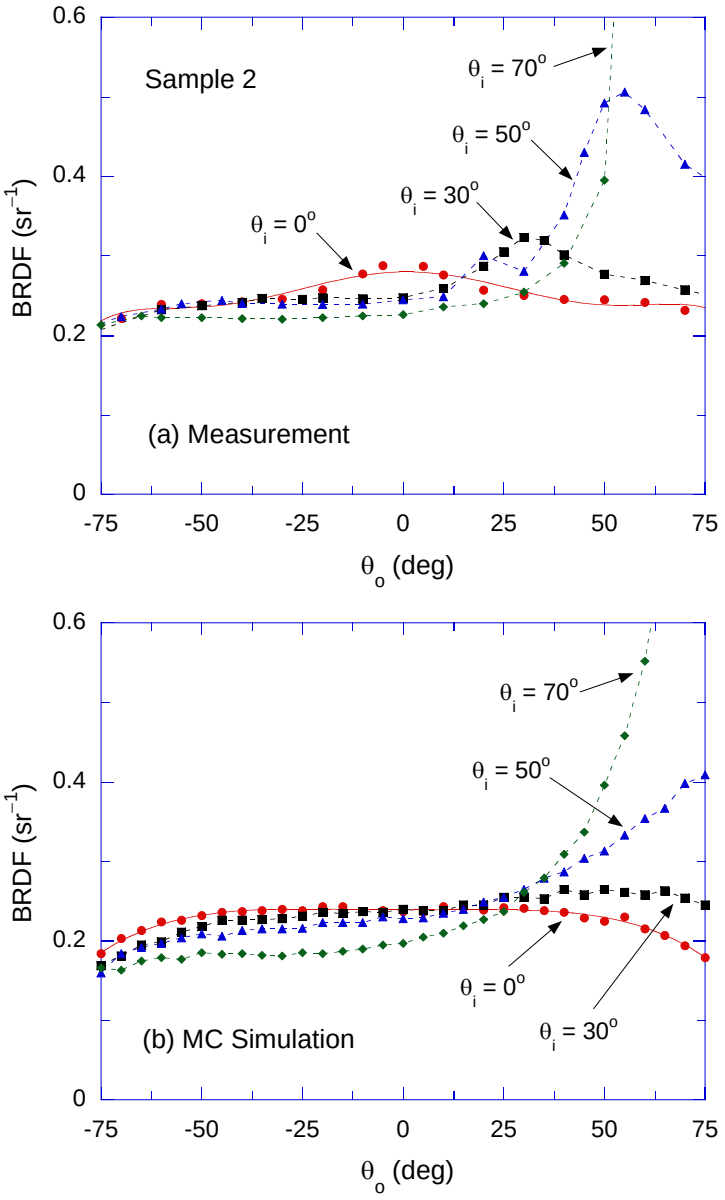


Figure 4.8 BRDF of Sample 2 at incidence angles of 0°, 30°, 50°, and 70°: (a) measurement; (b) Monte Carlo simulation. The symbols represent the measured and calculated values. The solid lines represent fitted curves of BRDF at normal incidence.

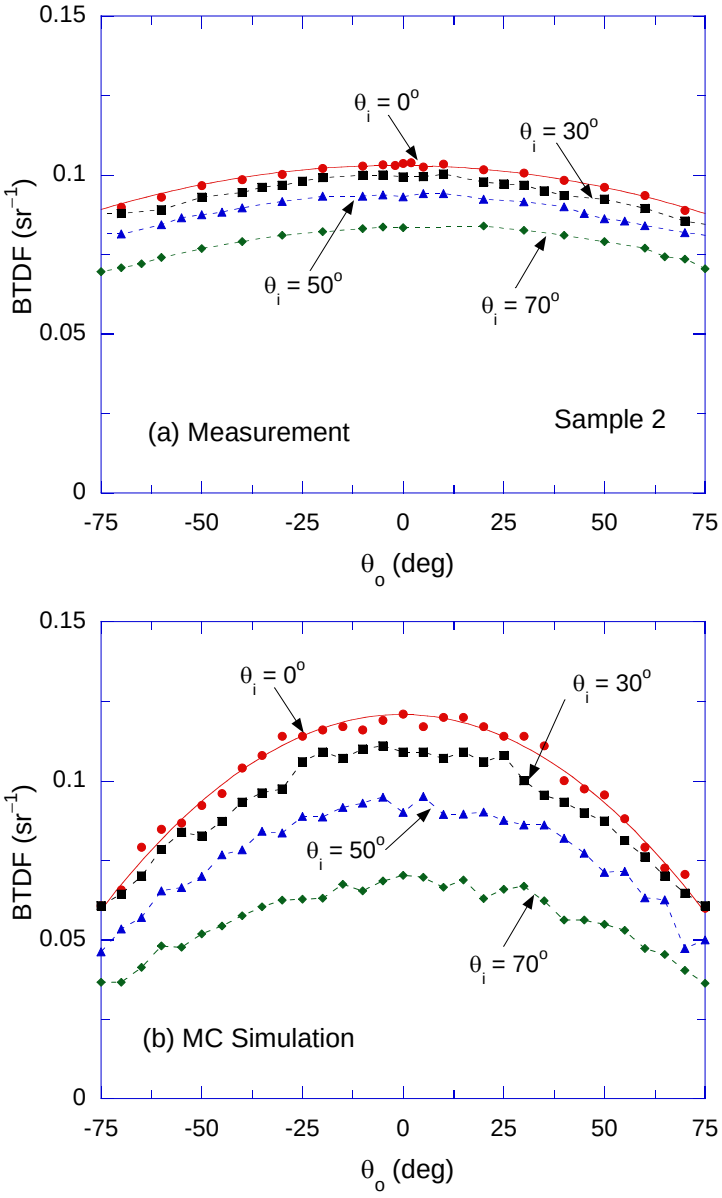


Figure 4.9 BTDF of Sample 2 at incidence angles of 0°, 30°, 50°, and 70°: (a) measurement; (b) Monte Carlo simulation. The symbols represent the measured and calculated values. The solid lines represent fitted curves of BTDF at normal incidence.

Figure 4.9 shows the measured and calculated BTDF of Sample 2 at various angles of incidence. The solid lines represent fitted polynomial curves of BTDF with a SEE less than $0.003\,\mathrm{sr}^{-1}$ for both the measured values and the calculated values. The BTDF decreases as the incidence angle increases. The noticeable feature of the BTDF is that it is symmetric with respect to $\theta_0 = 0°$ even at oblique incidence. This is because the volume scattering dominates the movement of transmitted photon bundles. When the photon bundles penetrate through the PTFE film, they have been redirected into random directions and are not affected by the incidence angle anymore after several scattering events. It should be noted that an attempt to unambiguously determine $\sigma$ and $g$ based on the bidirectional properties has been made. However, the calculation reveals that BRDF and BTDF, even at oblique incidence, are nearly insensitive to the asymmetric parameter $g$ in the range from 0.80 to 0.98 if the reduced scattering coefficient is fixed.

### 4.5 The Validity of Analytical Expressions of BRDF and BTDF

As discussed in Chapter 2, there are some analytical expressions of bidirectional properties, including the Hapke model, Pierce-Marcus formulae, and the Sobolev-Kokhanovsky model. However, there are some limitations associated with these analytical models. For the Hapke model, the medium is limited to infinite depth. The Pierce Marcus model requires the medium to be isotropic in scattering. Although the Sobolev-Kokhanovsky model does not limit the medium to be infinite depth or isotropic in scattering, there is no effective method to determine the two unknown parameters ($C_1$ and $C_2$ in Eq. (2.58)) in the model. However, if the scattering of the medium is isotropic,

then it follows that $C_1 = C_2 = 1$. Therefore, these analytical models become applicable if the PTFE material can be treated as an isotropic scattering medium.

Fortunately, since light scattering in the PTFE material is in the diffusion regime (i.e. scattering dominant regime), the medium can be treated as isotropic scattering by using the reduced scattering coefficient $\sigma' = \sigma(1-g) = 167\ \mathrm{cm}^{-1}$. As discussed earlier, the PTFE material is a highly forward scattering material with a scattering coefficient $\sigma$ greater than $1200\ \mathrm{cm}^{-1}$ and an asymmetric parameter *g* greater than 0.8. The movement of photon bundles inside the medium can be described by random walks of step size less than $1/\sigma = 8.3\times10^{-4}$ cm whose deflection angle is described by the scattering phase function. Equivalently, the diffusion of photon bundles can be described in a random walk of step size of $1/\sigma' = 6.0\times10^{-3}$ cm where each step involves isotropic scattering. Based on this reasoning, the PTFE will be treated as an effective medium that is isotropic scattering with a scattering coefficient of $167\ \mathrm{cm}^{-1}$ so as to apply the analytical expressions of BRDF and BTDF.

In the case of non-absorbing media, isotropic scattering, and infinite optical thickness, the BRDF expression can be expressed as

$$f_{\mathrm{r},\infty} = \frac{2(\mu+\mu_{\mathrm{i}}) + 4\mu\mu_{\mathrm{i}} + 1}{4\pi(\mu+\mu_{\mathrm{i}})} \tag{4.15}$$

where $\mu = \cos\theta$ and $\mu_{\mathrm{i}} = \cos\theta_{\mathrm{i}}$. This expression can be derived from all the analytical models including the Hapke model, Pierce-Marcus formulae, and the Sobolev-Kokhanovsky model discussed in Chapter 2.

If the optical thickness is finite, the Pierce-Marcus formulae express the BRDF and BTDF as

$$f_{\mathrm{r}} = \frac{1}{4\pi\left(\mu + \mu_{\mathrm{i}}\right)}\left[X(\mu)X(\mu_{\mathrm{i}}) - Y(\mu)Y(\mu_{\mathrm{i}})\right] \tag{4.16}$$

$$f_{\mathrm{t}} = \frac{1}{4\pi\left(\mu - \mu_{\mathrm{i}}\right)}\left[Y(\mu)X(\mu_{\mathrm{i}}) - X(\mu)Y(\mu_{\mathrm{i}})\right] \tag{4.17}$$

where both the $X$ and $Y$ functions, given in Eqs.(2.41) and (2.42), are functions of optical thickness. According to the Sobolev-Kokhanovsky model, the BRDF and BTDF are given as

$$f_{\mathrm{r}} = f_{\mathrm{r},\infty} - f_{\mathrm{t}} \tag{4.18}$$

$$f_{\mathrm{t}} = \frac{K_0(\mu)K_0(\mu_{\mathrm{i}})}{\pi\left[0.75\tau + \Delta\right]} \tag{4.19}$$

where $\tau$ is the optical thickness, $\Delta = 3\int_0^1 K_0(\mu)\mu^2 d\mu$, and $K_0(\mu)$ can be approximated by $K_0(\mu) \approx \frac{3}{7}(1+2\mu)$.

Figure 4.10 shows both the Monte Carlo simulation and the Sobolev-Kokhanovsky modeling of the BRDF of Samples 1 to 5 at normal incidence. The dots and the lines represent the Monte Carlo simulation and the Sobolev-Kokhanovsky model, respectively. As in previous section, the parameters used in the Monte Carlo simulation are $\sigma' = 167\,\mathrm{cm}^{-1}$ and $g = 0.9$. For the analytical model, the parameters are set as $\sigma = 167\,\mathrm{cm}^{-1}$ and $g = 0$ (i.e. isotropic scattering). In diffusion regime, the parameter settings used in the Monte Carlo simulation are equivalent to that used in the analytical model. The analytical model agrees very well with the Monte Carlo simulation for all the

samples except for observation angles larger than 60°. The deviation at large observation angle increases as the sample thickness decreases.

Figure 4.11 shows both the Monte Carlo simulation and the Sobolev-Kokhanovsky model of the BTDF of Samples 1 to 4 at normal incidence. The dots and the lines represent the Monte Carlo simulation and the Sobolev-Kokhanovsky model, respectively. The parameters used in the Monte Carlo simulation and the analytical model are the same as in Figure 4.10. The analytical model agrees very well with the Monte Carlo simulation for all the samples in the entire range of observation angle. The deviation at large observation angle shown in the BRDF modeling does not appear in the BTDF modeling. Comparing with the Monte Carlo simulation, the analytical model is able to predict the BTDF with similar accuracy, but much higher efficiency in calculation.

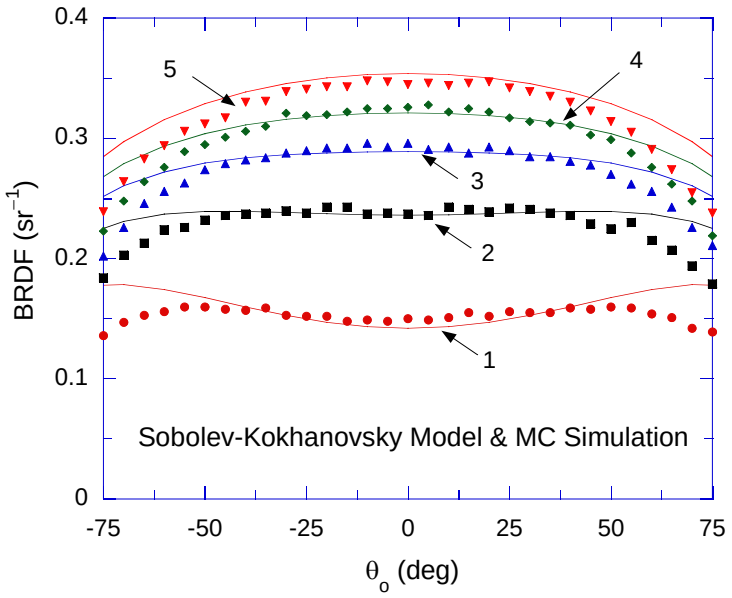


Figure 4.10 Comparison between the Monte Carlo simulation of the BRDF of Samples 1-5 and the analytical model of BRDF (Sobolev-Kokhanovsky Model) at normal incidence. The dots represent the Monte Carlo simulation. The lines represent the analytical model.

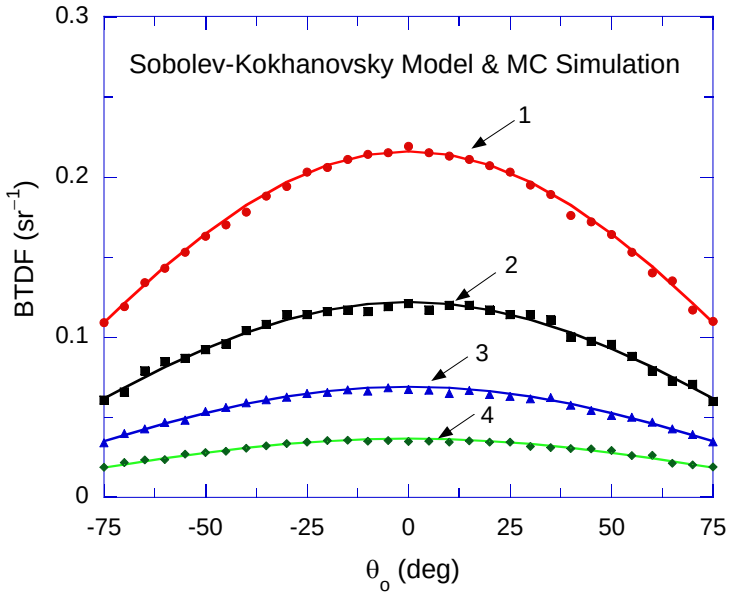


Figure 4.11 Comparison between the Monte Carlo simulation of the BTDF of Samples 1-4 and the analytical model of BTDF (Sobolev-Kokhanovsky Model) at normal incidence. The dots represent the Monte Carlo simulation. The lines represent the analytical model.

Figure 4.12 shows both the Monte Carlo simulation and the Pierce-Marcus model of the BRDF of the samples at normal incidence. The dots and the lines represent the Monte Carlo simulation and the analytical model, respectively. Again, the parameters used in the Monte Carlo simulation and the analytical model are the same as that in Figure 4.10. The analytical model agrees very well with the Monte Carlo simulation for Samples 2-5 except for observation angles larger than 60°. However, the analytical model deviates from the Monte Carlo model significantly for Sample 1 which is the thinnest sample.

Figure 4.13 shows both the Monte Carlo simulation and the Pierce-Marcus model of the BTDF of the samples at normal incidence. The analytical model agrees very well with the Monte Carlo simulation for Samples 2-5. Again, the Pierce-Marcus model cannot match the Monte Carlo simulation for Sample 1.

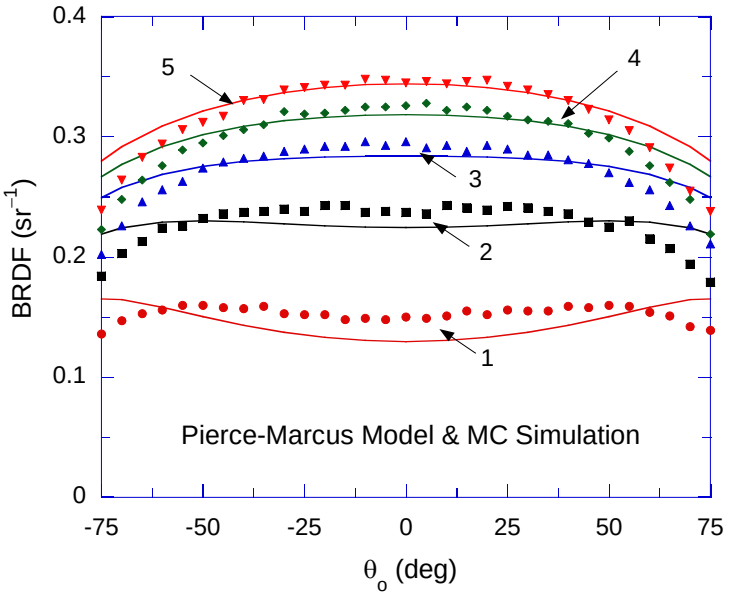


Figure 4.12 Comparison between the Monte Carlo simulation of the BRDF of Samples 1-5 and the analytical model of BRDF (Pierce-Marcus Model) at normal incidence. The dots represent the Monte Carlo simulation. The lines represent the analytical model.

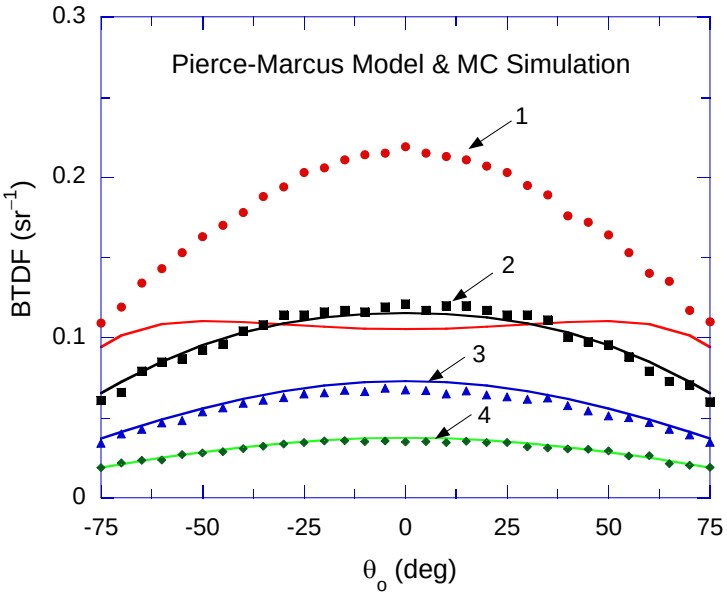


Figure 4.13 Comparison between the Monte Carlo simulation of the BTDF of Samples 1-4 and the analytical model of BTDF (Pierce-Marcus model) at normal incidence. The dots represent the Monte Carlo simulation. The lines represent the analytical model.

For Samples 2 to 5, both the Pierce-Marcus formulae and the Sobolev-Kokhanovsky model can provide similar accuracy in the prediction of BRDF and BTDF at normal incidence. For samples as thin as Sample 1, the Pierce-Marcus formulae produce significant error in the prediction of BRDF and BTDF. However, the accuracy of the Sobolev-Kokhanovsky model does not deteriorate even when the optical thickness of the sample reduces to a magnitude similar to Sample 1. Under appropriate scattering regime, these analytical models are not only highly efficient in calculation but also similar in accuracy as Monte Carlo simulation. It should be noted that these models are effective for normal incidence only.

### 4.6 Wavelength Dependence of the Directional-Hemispherical Properties

The directional-hemispherical reflectance and transmittance of the PTFE films were measured using the system of monochromator and integrating sphere. The wavelength ranges from 400 nm to 700 nm. The background signal was obtained by shooting the light on to the inner wall of the integrating sphere without attaching any sample onto it. For the measurement of the reflectance, the PTFE films were placed on the port on the backside of the integrating sphere. For the measurement of the transmittance, the PTFE films were placed on the entrance port of the integrating sphere.

As shown in Fig. 4.14, as the thickness of the sample increases the reflectance increases, and the transmittance decreases. The reflectance of the 10 mm slab is approximately unity across the wavelength range. For all the thinner samples, as the wavelength increases the reflectance decreases, and the transmittance increases. It seems that both the reflectance and transmittance are in linear relationship with the wavelength.

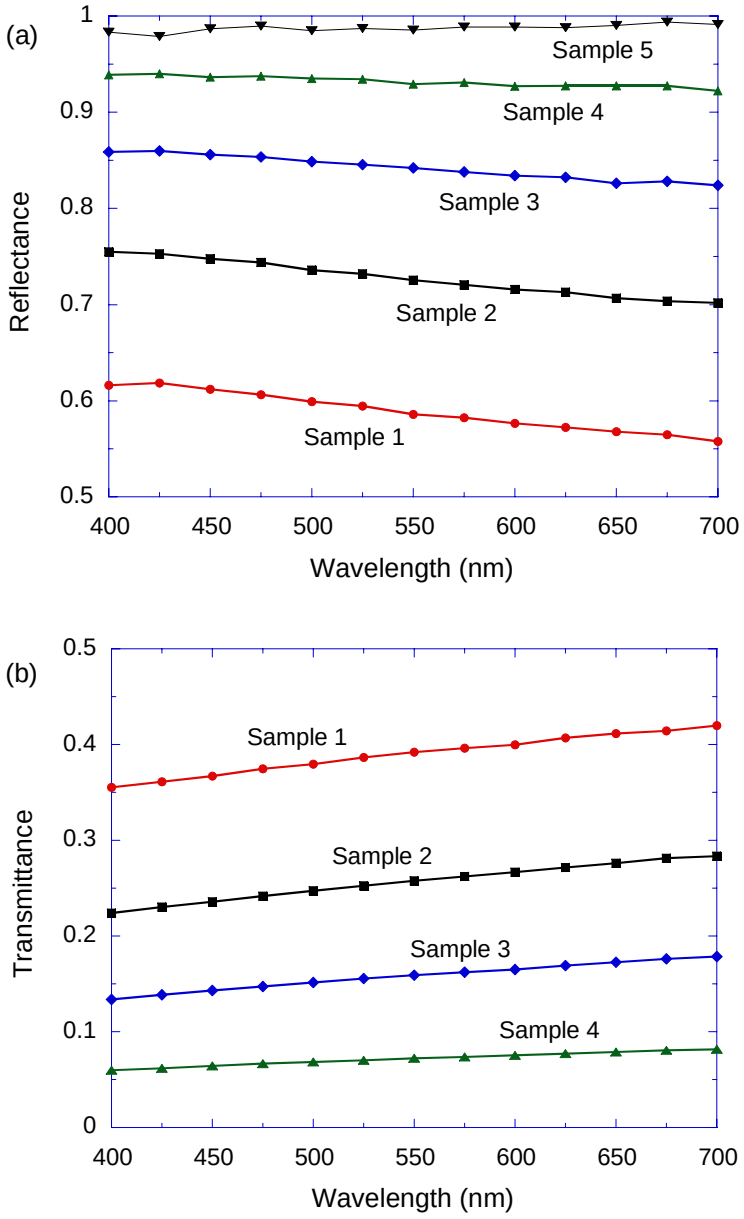


Figure 4.14 Directional-hemispherical reflectance and transmittance of the PTFE samples measured using the integrating sphere system: (a) reflectance; (b) transmittance. The wavelength ranges from 400 nm to 700 nm in a 25 nm interval.

PTFE has been used as whiteness standard in colorimetry. The color of PTFE can be defined in the CIE XYZ chromaticity values which are calculated using the following equation.

$$\begin{cases} X = \int_{380}^{780} D65(\lambda)R(\lambda)\bar{x}(\lambda)d\lambda \\ Y = \int_{380}^{780} D65(\lambda)R(\lambda)\bar{y}(\lambda)d\lambda \\ Z = \int_{380}^{780} D65(\lambda)R(\lambda)\bar{z}(\lambda)d\lambda \end{cases} \tag{4.15}$$

where $D65(\lambda)$ is the light source, $R(\lambda)$ is the reflectance, and $\bar{x}(\lambda)$, $\bar{y}(\lambda)$, and $\bar{z}(\lambda)$ are the color-matching functions. The weights, X, Y, and Z define a color in the CIE XYZ space.

After projecting the space to the $X+Y+Z=1$ plane, the x and y values can be determined in the resulting 2D space (i.e. the CIE chromaticity diagram) using Eq. (4.16). In the CIE chromaticity diagram, the constant energy white point is located at $x=y=1/3$. The X, Y and Z values were determined based on the directional-hemispherical reflectance of PTFE films. The directional-hemispherical reflectance of each sample as a function of wavelength was determined by fitting the directional-hemispherical reflectance measurement in the range from 400 nm to 700 nm. Furthermore, this function can be extrapolated into the full visible range (i.e. 380 nm to 780 nm). The (x, y) values of Samples 1 to 5 determined using Eqs. (15) and (16) are (0.309, 0.327), (0.310, 0.328), (0.312, 0.329), (0.313, 0.330), and (0.314, 0.331), respectively. Although there is slight variation of the x and y values as the sample thickness changes, these values are very close to the constant energy white point (i.e. $x=y=1/3$).

$$\begin{cases} x = \dfrac{X}{X+Y+Z} \\ y = \dfrac{Y}{X+Y+Z} \\ z = \dfrac{Z}{X+Y+Z} \end{cases} \tag{4.16}$$

Figure 4.15 shows the position of the color of PTFE in the CIE chromaticity diagram. The dot in the center of the diagram represents the color of PTFE. Due to its diffuse characteristics and its approximation to the white point, PTFE is used as whiteness standards in colorimetry [7,8].

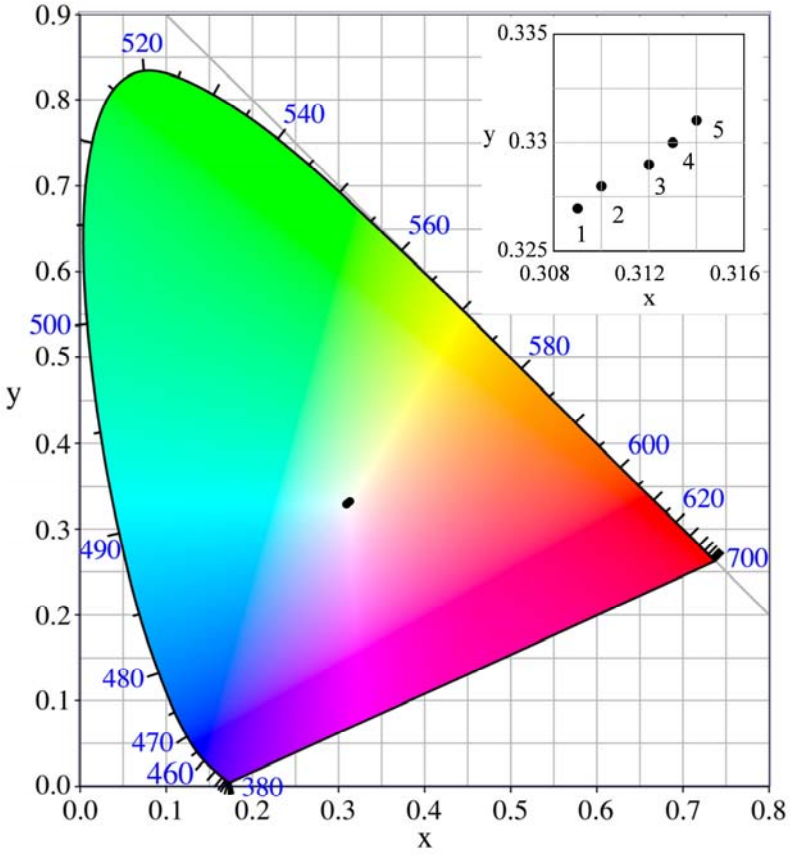


Figure 4.15 The color of PTFE in the CIE xy chromaticity diagram. The dots represent the x and y values of PTFE in the CIE chromaticity diagram. The numbers in the inset figure indicate the corresponding sample.

# CHAPTER 5

# CONCLUSIONS

The ranges of the RTE parameters of PTFE were determined by measuring the BRDF and BTDF of five PTFE films using a laser scatterometer. The directional-hemispherical reflectance and transmittance were derived by the integration of BRDF and BTDF data over the hemisphere. The ratio of the directional-hemispherical reflectance and transmittance of the samples were compared with the calculated values by using the adding-doubling method in order to determine the reduced scattering coefficient. It was found that the $R/T$ ratio linearly depends on the film thickness. The comparison shows that the reduced scattering coefficient of PTFE is $167\ \text{cm}^{-1}$. The lower limit of the scattering coefficient is determined as $1200\ \text{cm}^{-1}$ by analyzing the BTDF measurement of Sample 1 at normal incidence. The asymmetric parameter of the scattering phase function was estimated to be between 0.861 and 0.967, depending on the scattering coefficient. The absorption coefficient was determined to be less than $0.01\ \text{cm}^{-1}$.

Contrary to previously reported scattering coefficient and absorption coefficient of PTFE being similar to those of biological tissues, this study revealed that the scattering coefficient of PTFE is nearly 10 times greater than that of typical tissues while the absorption coefficient of PTFE is much less. The present study calls for careful distinction between the directly transmitted light and scattered light towards the direction parallel to the incidence. This is important for future research of light scattering in biological media for disease diagnostics and laser medicine.

While the directional-hemispherical properties agree well between the Monte Carlo simulation and adding-doubling method and also seem to be able to explain the experimental results, the BRDF and BTDF deviate significantly between simulation and measurements. Possible reasons are (1) scattering phase function of PTFE is much more complicated than the simple Henyey-Greenstein function; (2) there are coherent wave-like interactions that make it difficult to apply the RTE in such a highly scattering medium. Future studies are needed to understand the micro/nanostructures and how light interacts with PTFE.

# REFERENCES


[1] Weidner, V. R., Hsia, J. J., and Adams, B., 1985, "Laboratory Intercomparison Study of Pressed Polytetrafluoroethylene Powder Reflectance Standards," Applied Optics, **24**, pp. 2225-2230.

[2] McGuckin, B. T., Haner, D. A., and Menzies, R. T., 1997, "Multiangle Imaging Spectroradiometer: Optical Characterization of the Calibration Panels," Applied Optics, **36**, pp. 7016-7022.

[3] Bruegge, C. J., Stiegman, A. E., Rainen, R. A., and Springsteen, A. W., 1993, "Use of Spectralon as a Diffuse Reflectance Standard for in-Flight Calibration of Earth-Orbiting Sensors," Optical Engineering, **32**, pp. 805-814.

[4] Courreges-Lacoste, G. B., Schaarsberg, J. G., Sprik, R., and Delwart, S., 2003, "Modeling of Spectralon Diffusers for Radiometric Calibration in Remote Sensing," Optical Engineering, **42**, pp. 3600-3607.

[5] Stiegman, A. E., Bruegge, C. J., and Springsteen, A. W., 1993, "Ultraviolet Stability and Contamination Analysis of Spectralon Diffuse Reflectance Material," Optical Engineering, **32**, pp. 799-804.

[6] Weidner, V. R. and Hsia, J. J., 1981, "Reflection Properties of Pressed Polytetrafluoroethylene Powder," Journal of Optical Society of America, A, **71**, pp. 856-861.

[7] Fairchild, M. D. and Daoust, D. J. O., 1988, "Goniospectrophotometric Analysis of Pressed PTFE Powder for Use as a Primary Transfer Standard," Applied Optics, **27**, pp. 3392-3396.

[8] Kim, C.-S. and Kong, H.-J., 1997, "Rapid Absolute Diffuse Spectral Reflectance Factor Measurements Using a Silicon- Photodiode Array," Color Research and Application, **22**, pp. 275-279.

[9] Early, E. A., Barnes, P. Y., Johnson, B. C., Butler, J. J., Bruegge, C. J., Biggar, S. F., Spyak, P. R., and Pavlov, M. M., 1999, "Bidirectional Reflectance Round-Robin in Support of the Earth Observing System Program," Journal of Atmospheric and Oceanic Technology, **17**, pp. 1077-1091.

[10] Haner, D. A., McGuckin, B. T., and Bruegge, C. J., 1999, "Polarization Characteristics of Spectralon Illuminated by Coherent Light," Applied Optics, **38**, pp. 6350-6356.

[11] Voss, K. J. and Zhang, H., 2006, "Bidirectional Reflectance of Dry and Submerged Labsphere Spectralon Plaque," Applied Optics, **45**, pp. 7924-7927.

[12] Chandrasekhar, S., 1960, *Radiative Transfer*. Dover, New York, NY.

[13] Mudgett, P. S. and Richards, L. W., 1971, "Multiple Scattering Calculations for Technology," Applied Optics, **10**, pp. 1485-1502.

[14] Stamnes, K., Tsay, S.-C., Wiscombe, W., and Jayaweera, K., 1988, "Numerically Stable Algorithm for Discrete-Ordinate-Method Radiative Transfer in Multiple Scattering and Emitting Layered Media," Applied Optics, **27**, pp. 2502-2509.

[15] Evans, K. E., 1993, "Two-Dimensional Radiative Transfer in Cloudy Atmospheres: The Spherical Harmonic Spatial Grid Method," Journal of the Atmospheric Sciences, **50**, pp. 3111-3124.

[16] Mishchenko, M. I., Dlugach, J. M., Yanovitskij, E. G., and Zakharova, N. T., 1999, "Bidirectional Refectance of Flat, Optically Thick Particulate Layers: An Efficient Radiative Transfer Solution and Applications to Snow and Soil Surfaces," Journal of Quantitative Spectroscopy & Radiative Transfer, **63**, pp. 409-432.

[17] Bulgarelli, B., Kisselev, V. B., and Roberti, L., 1999, "Radiative Transfer in the Atmosphere–Ocean System: The Finite-Element Method," Applied Optics, **38**, pp. 1530-1542.

[18] Kisselev, V. B., Roberti, L., and Perona, G., 1994, "An Application of the Finite Element Method to the Solution of the Radiative Transfer Equation," Journal of Quantitative Spectroscopy & Radiative Transfer, **51**, pp. 545-663.

[19] Kisselev, V. B., Roberti, L., and Perona, G., 1995, "Finite-Element Algorithm for Radiative Transfer in Vertically Inhomogeneous Media: Numerical Scheme and Applications," Applied Optics, **34**, pp. 8460-8471.

[20] Ambirajan, A. and Look JR, D. C., 1996, "A Backward Monte Carlo Estimator for the Multiple Scattering of a Narrow Light Beam," Journal of Quantitative Spectroscopy & Radiative Transfer, **56**, pp. 317-336.

[21] Gjerstad, K. I., Stamnes, J. J., Hamre, B., Lotsberg, J. K., Yan, B., and Stamnes, K., 2003, "Monte Carlo and Discrete-Ordinate Simulations of Irradiances in the Coupled Atmosphere–Ocean System," Applied Optics, **42**, pp. 2609-2622.

[22] Howell, J. R., 1998, "The Monte Carlo Method in Radiative Heat Transfer," Journal of Heat Transfer, **120**, pp. 547-560.

[23] Roberti, L., 1997, "Monte Carlo Radiative Transfer in the Microwave and in the Visible: Biasing Techniques," Applied Optics, **36**, pp. 7929-7938.

[24] Chen, B., Stamnes, K., and Stamnes, J. J., 2001, "Validity of the Diffusion Approximation in Bio-Optical Imaging," Applied Optics, **40**, pp. 6356-6366.

[25] Contini, D., Martelli, F., and Zaccanti, G., 1997, "Photon Migration through a Turbid Slab Described by a Model Based on Diffusion Approximation. I. Theory," Applied Optics, **36**, pp. 4587-4599.

[26] Ishimaru, A., 1989, "Diffusion of Light in Turbid Material," Applied Optics, **28**, pp. 2210-2215.

[27] Wang, L. V., 1998, "Rapid Modeling of Diffuse Reflectance of Light in Turbid Slabs," Journal of Optical Society of America, A, **15**, pp. 936-944.

[28] Cheong, W.-F., Prahl, S. A., and Welch, A. J., 1990, "A Review of the Optical Properties of Biological Tissues," Journal of Quantum Electronics, **26**, pp. 2166-2185.

[29] Huber, N., Heitz, J., and Bauerle, D., 2004, "Pulsed-Laser Ablation of Polytetrafluoroethylene (Ptfe) at Various Wavelengths," The European Physical Journal Applied Physics, **25**, pp. 33-38.

[30] Schuster, A., 1905, "Radiation through Foggy Atmospheres," The Astrophysical Journal, **21**, pp. 1-22.

[31] Kubelka, P., 1948, "New Contributions to the Optics of Intensely Light-Scattering Materials. Part I," Journal of the Optical Society of America, **38**, pp. 448-457.

[32] Kubelka, P. and Munk, F., 1931, "An Article on Optics of Paint Layers," Z. Tech. Physik, **12**, pp. 593–601.

[33] Philips-Invernizzi, B., Dupont, D., and Caze, C., 2001, "Bibliographical Review for Reflectance of Diffusing Media," Optical Engineering, **40**, pp. 1082-1092.

[34] Duntley, S. Q., 1942, "The Optical Properties of Diffusing Materials," Journal of the Optical Society of America, **32**, pp. 61-70.

[35] Maheu, B. and Gouesbet, G., 1986, "Four-Flux Models to Solve the Scattering Transfer Equation: Special Cases," Applied Optics, **25**, pp. 1122-1128.

[36] Maheu, B., Letoulouzan, J. N., and Gouesbet, G., 1984, "Four-Flux Models to Solve the Scattering Transfer Equation in Terms of Lorenz-Mie Parameters," Applied Optics, **23**, pp. 3353-3362.

[37] Vargas, W. E. and Niklasson, G. A., 1997, "Generalized Method for Evaluating Scattering Parameters Used in Radiative Transfer Models," Journal of Optical Society of America, A, **14**, pp. 2243-2252.

[38] Plass, G. N., Kattawar, G., and Catchins, F., 1973, "Matrix Operator Theory of Radiative Transfer. 1: Rayleigh Scattering," Applied Optics, **12**, pp. 314-329.

[39] Brygo, F., Semerok, A., Weulersse, J.-M., and Thro, P.-Y., 2006, "Laser Ablation of a Turbid Medium: Modeling and Experimental Results," Journal of Applied Physics, **100**, pp. 033106.

[40] Ishimaru, A., 1978, *Wave Propagation and Scattering in Random Media*. Academic Press, London, Vol. 1.

[41] van de Hulst, H. C., 1980, *Multiple Light Scattering*. Academic Press, New York, Vol. 1.

[42] Prahl, S. A., van Gemert, M. J. C., and Welch, A. J., 1993, "Determining the Optical Properties of Turbid Media by Using the Adding-Doubling Method," Applied Optics, **32**, pp. 559-568.

[43] Prahl, S. A., "Light Transport in Tissue," vol. Ph.D. Austin, TX: The University of Texas at Austin, 1988.

[44] Hapke, B., 1981, "Bidirectional Reflectance Spectroscopy," Journal of Geophysical Research, **86**, pp. 3039-3054.

[45] Hapke, B., 2002, "Bidirectional Reflectance Spectroscopy 5. The Coherent Backscatter Opposition Effect and Anisotropic Scattering," Icarus, **157**, pp. 523-534.

[46] Hapke, B. and Wells, E., 1981, "Bidirectional Reflectance Spectroscopy 2. Experiments and Observations," Journal of Geophysical Research, **86**, pp. 3055-3061.

[47] Kokhanovsky, A. A., 2002, "Simple Approximate Formula for the Reflection Function of a Homogeneous, Semi-Infinite Turbid Medium," Journal of Optical Society of America, A, **19**, pp. 957-960.

[48] Kokhanovsky, A. A., 2004, *Light Scattering Media Optics*, Third ed. Praxis Publishing, Chichester, UK.

[49] Kokhanovsky, A. A. and Sokoletsky, L. G., 2006, "Reflection of Light from Semi- Infinite Absorbing Turbid Media. Part 2: Plane Albedo and Reflection Function," Color Research and Application, **31**, pp. 498-509.

[50] Sobolev, V. V., 1975, *Light Scattering in Planetary Atmospheres*, First ed. Pergamon Press, Oxford.

[51] Sobolev, V. V., 1984, "Integral Relations and Asymptotic Expressions in the Theory of Radiative Transfer," Astrofizika, **20**, pp. 123-132.

[52] Zhang, Z. M., 2007, *Nano/Microscale Heat Transfer*, First ed. McGraw-Hill, New York, NY.

[53] Pierce, P. E. and Marcus, R. T., 1997, "Radiative Transfer Theory Solid Color-Matching Calculations," Color Research and Application, **22**, pp. 72-87.

[54] Kokhanovsky, A. A., Nakajima, T., and Zege, E. P., 1998, "Physically Based Parameterizations of the Short-Wave Radiative Characteristics of Weakly Absorbing Optically Thick Media: Application to Liquid-Water Clouds," Applied Optics, **37**, pp. 4750-4757.

[55] Shen, Y. J., Zhu, Q. Z., and Zhang, Z. M., 2003, "A Scatterometer for Measuring the Bidirectional Reflectance and Transmittance of Semiconductor Wafers with Rough Surfaces," Review of Scientific Instruments, **74**, pp. 4885-4892.

[56] Lee, H. J., Bryson, A. C., and Zhang, Z. M., 2007, "Measurement and Modeling of the Emittance of Silicon Wafers with Anisotropic Roughness," International Journal of Thermophysics, **28**, pp. 918-932.

[57] van de Hulst, H. C., 1980, *Multiple Light Scattering*. Academic Press, New York, Vol. 2.

[58] Press, W. H., Flannery, B. P., Teukolsky, S. A., and Vetterling, W. T., 2002, *Numerical Recipes in C: The Art of Scientific Computing*, Second ed. Cambridge University, New York.

[59] Zhou, Y. H. and Zhang, Z. M., 2003, "Radiative Properties of Semitransparent Silicon Wafers with Rough Surfaces," Journal of Heat Transfer, **125**, pp. 462-470.

[60] Wang, L., Jacques, S. L., and Zheng, L., 1995, "Mcml - Monte Carlo Modeling of Light Transport in Multi-Layered Tissues," Computer Methods and Programs in Biomedicine, **47**, pp. 131-146.

[61] Star, W. M., Marijnissen, J. P. A., and van Gemert, M. J. C., 1988, "Light Dosimetry in Optical Phantoms and in Tissues," Physics in Medicine & Biology, **33**, pp. 437-454.

[62] Early, E. A., Barnes, P. Y., Johnson, B. C., Butler, J. J., Bruegge, C. J., Biggar, S. F., Spyak, P. R., and Pavlov, M. M., 2000, "Bidirectional Reflectance Round-Robin in Support of the Earth Observing System Program," Journal of Atmospheric and Oceanic Technology, **17**, pp. 1077-1091.

[63] Lee, H. J., Lee, B. J., and Zhang, Z. M., 2005, "Modeling the Radiative Properties of Semitransparent Wafers with Rough Surfaces and Thin-Film Coatings," Journal of Quantitative Spectroscopy & Radiative Transfer, **93**, pp. 185-194.

[64] Kokhanovsky, A. A. and Zege, E. P., 2004, "Scattering Optics of Snow," Applied Optics, **43**, pp. 1589-1602.